# Transcriptional initiation and mechanically driven self-propagation of a tissue contractile wave during axis elongation

Anais Bailles[1*], Claudio Collinet[1*§], Jean-Marc Philippe[1], Pierre-François Lenne[1], Edwin Munro[2] and Thomas Lecuit[1,3§]

1. Aix Marseille Université & CNRS, IBDM - UMR7288 & Turing Centre for Living Systems, Campus de Luminy Case 907, 13288, Marseille, France
2. Department of Molecular Genetics and Cell Biology, University of Chicago, Chicago, IL 60637, United States
3. Collège de France, 11 Place Marcelin Berthelot, Paris, France

* Equal contribution
§ Corresponding authors: claudio.collinet@univ-amu.fr, thomas.lecuit@univ-amu.fr

## Abstract

**Tissue morphogenesis emerges from coordinated cell shape changes driven by actomyosin contraction[1,2]. Spatial patterns of gene expression regionalize and polarize cell behaviours, such as apical constriction in the ventral mesoderm and cell intercalation in the lateral ectoderm in *Drosophila* [3]. Thus, tissue dynamics is largely governed genetically. Actomyosin networks display remarkable self-organized dynamics at the cellular level, such as pulses and flows[4,5]. However how genetic control and self-organization of actomyosin networks drive tissue-level morphogenesis is not well understood.**

**Here we report two phases and modalities of Rho1 and non-muscle MyosinII (MyoII) activation in the *Drosophila* posterior endoderm. First, Rho1/MyoII are induced apically in a spatially restricted primordium region via localized transcription of the GPCR ligand Fog. Second, a tissue-scale wave of Rho1/MyoII activation and apical constriction progresses anteriorly across the dorsal epithelium at a constant speed of 1 cell every 3 minutes. Remarkably, wave progression does not require gene transcription, and is also insensitive to perturbations in the level and pattern of Fog expression. Thus, while *fog* transcription initiates Rho1/MyoII activation in the primordium, Fog delivery does not govern wave dynamics. Instead, perturbing the mechanical environment of the endoderm impaired MyoII wave dynamics. MyoII inhibition blocked acute Rho1 activation and propagation. We propose that MyoII contractility provides both local feedback amplification and spatial coupling necessary for wave progression. Thus endoderm morphogenesis emerges from local transcriptional initiation and a mechanically driven cycle of cell contraction akin to a trigger-wave.**

In *Drosophila* the presumptive posterior endoderm consists of a circular domain of cells at the posterior pole of the embryo (Fig.1a). Similar to the mesoderm, Rho1 and MyoII-dependent apical constriction drives invagination of the posterior endoderm[6,7], but the mechanisms underlying its polarized movement towards the dorsal anterior remain unknown. To understand how MyoII drives endoderm morphogenesis we imaged MyoII (using an mCherry-tagged MyoII Regulatory Light Chain, MRLC::mCherry) together with a marker of cell contours (E-cadherin::GFP) on the dorsal and posterior side of the embryo (Fig.1b and Movie 1). During the first 6 minutes MyoII is activated in the medial-apical region of cells within a spatially defined domain referred to as the endoderm primordium and comprising 7±1 rows of cells extending from the posterior pole. In this region MyoII is pulsatile and triggers step-wise apical constriction of cells (Fig.1b top and 1c-d) as in the mesoderm[8]. But in the next 25 minutes, apical MyoII activation propagates anteriorly within the dorsal epithelium across a domain of 8±1 cells hereafter called the propagation region (Fig.1g). During each round of MyoII activation, cells undergo apical constriction and incorporate in the invaginating furrow (Fig.1b middle-bottom and 1c-d and f), causing the furrow to expand and move towards the anterior. Thus, the region where MyoII activation and apical constriction occur is not

spatially fixed but dynamic (Fig. 1f and h). This contrasts sharply with the mesoderm, where the domain of cells undergoing apical constriction is precisely defined by the fixed domain of expression of the mesodermal genes *twist* and *snail*[3,9].

We quantitatively characterized this process further by tracking cells over time and measuring MyoII intensity and apical cell shape. To analyze the movement of the activation wave front within the epithelium we plotted MyoII intensity and apical cell shape parameters as a function of time and initial cell position along the AP-axis (Fig.1i-k and Extended Fig.1e-f, see Methods and Extended Fig.1a-d). Heat-map kymograph representations of MyoII intensity and apical cell shape show that the activation wave moves with a constant speed of 2.2±0.2 µm/min (corresponding to one cell every ~3 min, Fig.1i) and is preceded by a wave of anisotropic cell deformation in which apical surface areas increase along the AP-axis (Fig.1k and Extended Fig.1e-f). Strikingly, the kinetics of MyoII recruitment are very different in the primordium and in the propagation region (Fig.1c-e). While cells in the primordium recruit MyoII and constrict apically in a step-wise manner (Fig.1d), as in the mesoderm[8], cells in the propagation region recruit MyoII in two-phases: first a low-level activation (hereafter called pre-activation) concomitant with the increase in apical surface (Fig. 1j-m and Movie 2); second an acute activation where MyoII reaches high levels with very rapid kinetics (Fig.1d-e and Fig.1l), significantly faster than cells in the primordium. This suggests potentially different mechanisms of MyoII activation in the propagating region and in the primordium.

In *Drosophila* the small GTPase Rho1 activates MyoII through the downstream kinase Rok[10-12]. We visualized Rho1 activation by imaging a Rho1-GTP biosensor, the Anillin Rho-Binding-Domain (RBD) fused to GFP[11], and a GFP-tagged Rok[10] together with MyoII::mCherry. We found that both Rho1-GTP and Rok are activated at high levels together with MyoII in cells of the propagation domain (Fig.1n-o and Extended Fig.1g-h and Movies 3 and 4). Thus a wave of Rho1, Rok and MyoII activation propagates across cells of the dorsal epithelium. This led us to investigate the mechanisms underlying the wave of activation.

The medial apical activation of MyoII in the endoderm primordium depends on localized transcription and secretion of the GPCR ligand Fog[7,13]. Fog expression at the embryo posterior is controlled by the maternal terminal patterning system through the activity of the receptor tyrosine kinase Torso (Tor) and its target transcription factors Huckebein (Hkb) and Tailless (Tll)[7,14,15] (Fig.2a). In loss of function mutants for *tor* or *fog* or for *concertina*, which codes for the G-protein $G\alpha_{12/13}$ downstream of GPCRs[13], MyoII apical activation was abolished in the primordium, as expected, but also in cells of the propagation region (Fig.2b and Movie 5). We thus tested whether the expression of the endodermal genes *hkb* and *tll* and their downstream target *fog* propagates anteriorly within the dorsal epithelium to activate MyoII in cells of the propagation region (Fig.2a). Mid-sagittal sections (where the expression profile is best seen) of immunolabelled embryos revealed that Fog is present in the primordium region and that Tll is expressed in a larger region encompassing ~4 more cells towards the anterior (Fig.2c primordium contraction stages). The regions of expression of these two genes did not expand over time and their anterior boundaries were found in increasingly deeper positions of the invaginating furrow as new cells were incorporated (Fig.2c MyoII propagation stages). In contrast MyoII was enriched at cell apices at the invaginating front at all stages (Extended Fig.2a), reflecting anterior propagation of its activation. To confirm these data, we monitored *fog* transcription in living embryos together with MyoII using the MS2/MCP system[16]. Fog transcripts containing MS2 stem loops in the 3'UTR (see materials and methods) were detected as bright GFP dots in the nucleus marked with His2B::RFP. *fog* expression was detected in the primordium region at the end of cellularization and during the initial primordium contraction but did not propagate anteriorly over time along with MyoII activation (Fig.2d, Extended Fig.2b and Movie 6).

Together these data indicate that while MyoII activation in the primordium depends on localized transcription of the GPCR ligand Fog, the subsequent wave is not associated with activation of *fog* transcription in the propagation zone. Although *fog* transcription was not detected in the

propagation region, it is possible that transcription of other genes might work as part of a relay mechanism to propagate MyoII activity. To test this, we injected embryos with α-amanitin, a potent inhibitor of RNA Polymerase-II. Injection at the end of cellularization, when the pattern of expression of Tll and Fog is fully established, led to a rapid disappearance (within 2-3 mins) of nuclear foci of nascent Fog transcripts labelled with MS2/MCP::GFP (Extended Fig.2c and Movie 7). Remarkably, however, the wave of MyoII proceeded at a normal velocity (Fig.2e,f and Movie 8). Two processes requiring acute transcription during the same time window were affected, further confirming α-amanitin inhibitory activity: 1) cell divisions in mitotic domains (dependent on *cdc25*$^{string}$ transcription[17]) were blocked and 2) cell intercalation and planar polarized MyoII cables which require *even-skipped* and *toll2,6,8* transcription in the ventral lateral ectoderm were inhibited (Extended Fig.2d and Movie 8). These experiments demonstrate that while MyoII wave is initiated by *fog* transcription in the primordium, its progression depends on a relay mechanism not involving gene transcription.

Fog is thought to act through paracrine signalling[7]. Thus, in principle, the spread of Fog away from the primordium region, where it is produced and secreted, could underlie propagation of Rho1 and MyoII activity. Consistent with this general possibility, immuno-stained Fog protein was detected, albeit at low levels, at the apex of cells in the propagation zone close to the furrow (Extended Fig.3a). Simple models for diffusive spread of secreted ligands predict a wave front that flattens away from the source, which is inconsistent with the kinematics that we observe experimentally (Fig.1i). Extending earlier work[18,19]. a model that couples Fog diffusion and saturable receptor binding to MyoII activation can produce a travelling wave of sharp MyoII activity (Fig.3a,b and Extended Fig.3b). This model predicts faster propagation with higher rates of ligand production (Fig.3b and Extended Fig.3c). To challenge this hypothesis, we experimentally increased Fog expression in the primordium using 2 extra copies of *fog* under the control of the *hkb* promoter[20], and measured MyoII activation (Fig.3c-e Extended Fig.3c and Movie 9). In the primordium, MyoII was recruited earlier and its maximum levels were increased by ~20%. Maximum MyoII levels were also increased by ~10% in the propagation region, confirming a non-cell autonomous effect of Fog (Fig.3f), but, contrary to model predictions, the rapid switch to high MyoII levels in the propagation region occurred at the same time as in controls (Fig.3e), such that no change in wave speed was observed (Fig.3g and Extended Fig.3d). This indicates that source-limited diffusive spread of Fog is not the rate-limiting factor for MyoII propagation.
A wave of Fog signalling patterned by other mechanisms (e.g. ligand transport or GPCR regulation) might be required to activate MyoII in cells of the propagation region via GPCRs/Rho1 signalling. To test this we first overexpressed Fog uniformly in the embryo, overriding the endogenous Fog pattern (Fig.3h,i, Movie 10 and Extended Fig.3f). Under these conditions, although MyoII levels in the dorsal epithelium were increased, the global tissue-level pattern with high MyoII in the primordium and low MyoII in the amniosierosa was preserved (tissue polarity >0,5, Fig.3j). The MyoII pattern was similar when Fog was expressed uniformly in a *fog-/-* background (Extended Fig.3g-h), showing that this pattern was not due to endogenous *fog*., The transition from low to fully activated MyoII levels propagated anteriorly at similar speed and across a similar number of cells as in WT embryos (Fig.3k). Strikingly, the tissue-level polarity of MyoII was also maintained and propagation still occurred (Fig.3j,k and Movie 10) when the constitutively active forms of the GPCRs downstream targets $G\alpha_{12/13}$ and Rho1 were uniformly expressed (Fig.3h,i), indicating that bypassing GPCR regulation does not prevent wave propagation.
Altogether, these data argue that patterned Fog signaling does not determine the dynamics of MyoII wave propagation. Fog signalling may induce MyoII activation at low levels in cells of the propagation domain, but the switch to high MyoII levels (full activation) is not set solely by activation of the Fog-Rho1 pathway.

Since MyoII has been has been proposed to respond to mechanical stimuli[21,22] we considered the possibility that mechanical feedback (forces/stresses or cell deformation) could be involved in

propagating acute activation of MyoII across the tissue. Consistent with this view, before recruiting MyoII, cells in the propagation region are deformed anisotropically, i.e. their apical surface and aspect ratio change (Fig.1k and Extended Fig.1e-f), and thus they are subjected to anisotropic tension, as indicated by laser ablation experiments (Extended Fig.4a-c). To test the effect of mechanical regulation on wave propagation and see if MyoII-dependent tissue deformation was required to trigger the Rho1-GTP wave, we injected embryos with a Rok inhibitor (H-1152) and monitored the dynamics of Rho1-GTP with the biosensor (Anillin(RBD)::GFP). In injected embryos, the activation of Rho1 within the primordium (where Fog is expressed and secreted) was unaffected, but the propagation of Rho1 activity was sharply reduced to ~4 cell rows during the next 25-30 min (Fig.4a,b and Movies 11 and 12). This indicates that MyoII-dependent contraction in the primordium is required for normal propagation of Rho1, and hence activation of MyoII.
Next, we perturbed the mechanical environment of the dorsal epithelium using either mechanical or genetic perturbations that do not affect the genetic identity of endoderm cells. Using a previously characterized cauterization technique[23,24] we generated mechanical fences whereby cells are stitched to the fixed vitelline membrane. Medio-lateral cauterizations at ~30% egg length in the dorsal epithelium, namely ~20-30 cells anterior to the primordium, resisted the anterior movement of the posterior endoderm perturbing the normal mechanics of the tissue (Fig.4c middle-bottom panel and Movie 13). In dorsalized embryos, laid by *dorsal* mutant mothers, DV polarity is abolished and MyoII-dependent apical constriction in the endoderm primordium is rotationally symmetric, thus blocking endoderm movements towards the anterior and perturbing the normal mechanics of the tissue (Fig.4c right-bottom panel and Movie 14). Strikingly, in both cases the activation wave slowed down (Fig.4d-e and Movie 13) and cells recruited higher levels of MyoII compared to WT embryos (Fig.4f). Furthermore, the rate of cell apical constriction following MyoII recruitment in the propagation region was significantly reduced despite higher MyoII levels (Fig.4g-h), indicating a higher resistance to invagination. Importantly, similar perturbations by mechanical fences in the lateral ectoderm did not affect characteristic features of subcellular MyoII activation (i.e. frequency of medio-apical MyoII pulses and planar polarity[23]) thus revealing a specific mechanical sensitivity of dorsal-posterior epithelial cells. Altogether, these experiments reveal mechanical control over MyoII levels and wave speed in the propagation region.

The sensitivity of propagation speed and MyoII levels to conditions that perturb tissue-level mechanics led us to consider cell shape changes in 3D during propagation. Imaging in cross-sections revealed a striking cycle of 3D cell deformations that accompany MyoII propagation (Fig.4i and 4n). Cells in the row immediately anterior to the invaginating front became highly curved below the apical surface as they were pushed anteriorly and then upward by invaginating posterior endoderm cells (Fig.4i yellow cell in the top panel and Movie 15). As they moved upwards, cells appeared to attach and spread their apices against the vitelline membrane, resulting in the observed anisotropic cell area increase (Fig. 1k and Extended Fig.1e-f). Finally, cells activated apical MyoII, and constricted apically to join the invagination (Fig.4i bottom panel and Movie 15), thereby completing the cycle and expanding the invagination front by one row of cells towards the anterior. This in turn induced further anterior compression of the next row of cells in the propagation region and started a new cycle of 3D cell deformations (Movie 15). Two additional observations substantiated the idea that cells in the propagation region undergo a cycle of attachment and detachment from the vitelline membrane as they are deformed by the advancing invagination. First, we injected fluorescent 10kDa Dextran in the perivitelline space and measured its intensity across the dorsal epithelium as a proxy for the free space between cells and vitelline membrane. A gradient of intensity reached a minimum ahead of the invagination where cells increase their apical surface area, before activating activating MyoII (Extended Fig.4e-f). Second, we observed occasional cases of cells resisting detachment before being incorporated in the invagination (Extended Fig. 4g and Movie 17), indicating their physical contact with the overlaying vitelline membrane.

The speed of this mechanical cycle (estimated from the cell 3D deformation wavefront using both the apical cell area and the cell position along the apico-basal axis of the tissue, see Methods) and the speed of MyoII activation wave were highly correlated (Fig.4j-l) suggesting they are tightly linked. Indeed, the cycle of deformations was blocked instantly when MyoII was inhibited by injection of a Rok inhibitor during MyoII propagation (Fig.4m and Movie 16), indicating that it is mechanically self-propagating.
Thus, cells in the propagation domain undergo a self-replicating mechanical cycle of 3D cell deformations involving adhesion and apex spreading onto the vitelline membrane, followed by de-adhesion, MyoII activation and apical constriction.

To this point, our data suggest that wave propagation depends on a mechanical relay mechanism whereby each row of cells activates MyoII and invaginates, propagating global tissue deformations to cell neighbours causing their MyoII activation. To further understand the mechanical basis for wave propagation in this system, we modeled the tissue as an active contractile viscous material with local stress-dependent activation of MyoII[25] (Fig.5a). Simulations confirmed that two key elements are minimally sufficient for propagation of an activation-contraction wave in this model: 1) a non-linear positive feedback, in which stress locally activates MyoII and MyoII locally generates contractile stress and 2) a spatial coupling mechanism, in which MyoII activation in one cell generates stress in the neighbouring cells, thereby triggering MyoII activation there (Fig.5b,c). Lack of either of these elements would block wave propagation because 1) MyoII activity would not be amplified beyond a threshold once initiated in a cell and 2) because activation would fail to propagate from cell to cell.
To test experimentally whether these two elements are involved in propagating Rho1-GTP/MyoII activity and to assess whether contractility is required to sustain Rho1 activation in cells, we injected the Rok inhibitor H-1152 during propagation. This immediately blocked the rapid increase of Rho1 activity in cells in the process of activation (Fig.5d-g and Movie 18), thus confirming the local positive feedback loop of contractility onto Rho1 activity. Moreover, in cells not yet activated at the time of injection propagation of Rho1 activation across the tissue slowed down dramatically with kinetics that resembled diffusive spread, rather than wave propagation (Extended Fig.5 and Movie 19), possibly due to Fog signalling. Altogether, these results reveal the existence of both a cell-intrinsic (local feedback amplification) and a cell-extrinsic (spatial coupling) feedback of contractility onto Rho1GTP.

We conclude that the propagation of MyoII activation across the dorsal endoderm emerges from a genetically determined initiation phase and a mechanically relayed self-organized activation wave. Initiation stems from a Fog-based genetic signalling in the endoderm primordium. Fog transcription is spatially controlled by the Torso-dependent terminal system and this induces Rho1 and MyoII activation and apical constriction. This is followed by propagation of a wave of activation independent of transcription and based on a mechanical feedback amplification and spatial coupling mechanism (Fig. 5h), similar to trigger waves[26,27]. Our hypothesis is that chemical signalling (e.g. Fog) induces a state of low cortex activation (MyoII pre-activation), onto which mechanical stimuli above a critical threshold trigger an irreversible transition to a high activity state. MyoII inhibition leaves cells below this threshold (Extended Fig.5). Mechanical stimuli could act via direct MyoII motor stabilization by strain/stress [28,29], membrane tension [30], and/or contact with the vitelline membrane.
The *Drosophila* embryo is a remarkable example of genetic control over cell mechanics: activation of MyoII is spatially controlled and polarized by tight control over expression of regulators of contractility[3]. Our observations reveal that once initiated genetically, remarkable spatial pattern and dynamics also emerge through mechanical control and self-organization. This is a striking example of how a tight spatial and temporal control of cell behaviour within a tissue arises via mechanical signals. This work opens the door to a deeper investigation of how mechano-chemical signalling not

only induces cell shape changes but also gives rise to spatiotemporal patterns of deformation at the tissue level.

## Author Contributions

A.B., C.C. and T.L conceived the project and planned experiments. A.B and C.C. performed all experiments and quantifications. A.B. did the simulations and discussed them with E.M. J-M.P. designed the MS2-fog construct and all other Sqh::mCherry and mKate2 constructs. A.B., C.C. and T.L. analysed the results and discussed them with E.M. P-F.L. gave inputs. A.B., C.C. and T.L. wrote the manuscript and all authors made comments.

## Acknowledgements

We thank all members of the Lecuit and Lenne group for stimulating and useful discussions during the course of this project. We thank the IBDM imaging facility for assistance with maintenance of the microscopes, FlyBase for maintaining curated databases and Bloomington for providing fly stocks. This work was supported by the ERC grant Biomecamorph #323027). C.C. was supported by the CNRS, A.B. was supported by Excellence Initiative of Aix-Marseille University - A*MIDEX, a French “Investissements d’Avenir” programme”. We acknowledge the France-BioImaging infra-structure supported by the French National Research Agency (ANR–10–INBS-04-01, «Investments for the future»).

## Competing financial interests

The authors declare no competing financial interests

# References


1 Lecuit, T. & Lenne, P. F. Cell surface mechanics and the control of cell shape, tissue patterns and morphogenesis. *Nat Rev Mol Cell Biol* **8**, 633-644, doi:10.1038/nrm2222 (2007).

2 Heisenberg, C. P. & Bellaiche, Y. Forces in tissue morphogenesis and patterning. *Cell* **153**, 948-962, doi:10.1016/j.cell.2013.05.008 (2013).

3 Gilmour, D., Rembold, M. & Leptin, M. From morphogen to morphogenesis and back. *Nature* **541**, 311-320, doi:10.1038/nature21348 (2017).

4 Levayer, R. & Lecuit, T. Biomechanical regulation of contractility: spatial control and dynamics. *Trends Cell Biol* **22**, 61-81, doi:10.1016/j.tcb.2011.10.001 (2012).

5 Bement, W. M. *et al.* Activator-inhibitor coupling between Rho signalling and actin assembly makes the cell cortex an excitable medium. *Nature Cell Biology* **17**, 1471-1483, doi:10.1038/ncb3251 (2015).

6 Sweeton, D., Parks, S., Costa, M. & Wieschaus, E. Gastrulation in Drosophila: the formation of the ventral furrow and posterior midgut invaginations. *Development* **112**, 775-789 (1991).

7 Costa, M., Wilson, E. T. & Wieschaus, E. A putative cell signal encoded by the folded gastrulation gene coordinates cell shape changes during Drosophila gastrulation. *Cell* **76**, 1075-1089 (1994).

8 Martin, A. C., Kaschube, M. & Wieschaus, E. F. Pulsed contractions of an actin-myosin network drive apical constriction. *Nature* **457**, 495-499, doi:10.1038/nature07522 (2009).

9 Leptin, M. & Roth, S. Autonomy and non-autonomy in Drosophila mesoderm determination and morphogenesis. *Development* **120**, 853-859 (1994).

10 Mason, F. M., Tworoger, M. & Martin, A. C. Apical domain polarization localizes actin-myosin activity to drive ratchet-like apical constriction. *Nat Cell Biol* **15**, 926-936, doi:10.1038/ncb2796 (2013).

11 Munjal, A., Philippe, J. M., Munro, E. & Lecuit, T. A self-organized biomechanical network drives shape changes during tissue morphogenesis. *Nature* **524**, 351-355, doi:10.1038/nature14603 (2015).

12 Kerridge, S. *et al.* Modular activation of Rho1 by GPCR signalling imparts polarized myosin II activation during morphogenesis. *Nat Cell Biol* **18**, 261-270, doi:10.1038/ncb3302 (2016).

13 Dawes-Hoang, R. E. *et al.* folded gastrulation, cell shape change and the control of myosin localization. *Development* **132**, 4165-4178, doi:10.1242/dev.01938 (2005).

14 Casanova, J. & Struhl, G. Localized Surface-Activity of Torso, a Receptor Tyrosine Kinase, Specifies Terminal Body Pattern in Drosophila. *Gene Dev* **3**, 2025-2038, doi:DOI 10.1101/gad.3.12b.2025 (1989).

15 Weigel, D., Jurgens, G., Klingler, M. & Jackle, H. Two gap genes mediate maternal terminal pattern information in Drosophila. *Science* **248**, 495-498 (1990).

16 Garcia, H. G., Tikhonov, M., Lin, A. & Gregor, T. Quantitative imaging of transcription in living Drosophila embryos links polymerase activity to patterning. *Curr Biol* **23**, 2140-2145, doi:10.1016/j.cub.2013.08.054 (2013).

17 Momen-Roknabadi, A., Di Talia, S. & Wieschaus, E. Transcriptional Timers Regulating Mitosis in Early Drosophila Embryos. *Cell Rep* **16**, 2793-2801, doi:10.1016/j.celrep.2016.08.034 (2016).

18 Kerszberg, M. & Wolpert, L. Mechanisms for positional signalling by morphogen transport: a theoretical study. *J Theor Biol* **191**, 103-114, doi:10.1006/jtbi.1997.0575 (1998).

19 Lander, A. D., Nie, Q. & Wan, F. Y. Do morphogen gradients arise by diffusion? *Dev Cell* **2**, 785-796 (2002).

20 Seher, T. C., Narasimha, M., Vogelsang, E. & Leptin, M. Analysis and reconstitution of the

genetic cascade controlling early mesoderm morphogenesis in the Drosophila embryo. *Mech Dev* **124**, 167-179, doi:10.1016/j.mod.2006.12.004 (2007).

21 Mitrossilis, D. *et al.* Mechanotransductive cascade of Myo-II-dependent mesoderm and endoderm invaginations in embryo gastrulation. *Nat Commun* **8**, 13883, doi:10.1038/ncomms13883 (2017).

22 Fernandez-Gonzalez, R., Simoes Sde, M., Roper, J. C., Eaton, S. & Zallen, J. A. Myosin II dynamics are regulated by tension in intercalating cells. *Dev Cell* **17**, 736-743, doi:10.1016/j.devcel.2009.09.003 (2009).

23 Collinet, C., Rauzi, M., Lenne, P. F. & Lecuit, T. Local and tissue-scale forces drive oriented junction growth during tissue extension. *Nat Cell Biol* **17**, 1247-1258, doi:10.1038/ncb3226 (2015).

24 Rauzi, M. *et al.* Embryo-scale tissue mechanics during Drosophila gastrulation movements. *Nat Commun* **6**, 8677, doi:10.1038/ncomms9677 (2015).

25 Odell, G. M., Oster, G., Alberch, P. & Burnside, B. The mechanical basis of morphogenesis. I. Epithelial folding and invagination. *Dev Biol* **85**, 446-462 (1981).

26 Gelens, L., Anderson, G. A. & Ferrell, J. E., Jr. Spatial trigger waves: positive feedback gets you a long way. *Mol Biol Cell* **25**, 3486-3493, doi:10.1091/mbc.E14-08-1306 (2014).

27 Allard, J. & Mogilner, A. Traveling waves in actin dynamics and cell motility. *Curr Opin Cell Biol* **25**, 107-115, doi:10.1016/j.ceb.2012.08.012 (2013).

28 Kovacs, M., Thirumurugan, K., Knight, P. J. & Sellers, J. R. Load-dependent mechanism of nonmuscle myosin 2. *Proc Natl Acad Sci U S A* **104**, 9994-9999, doi:10.1073/pnas.0701181104 (2007).

29 Heissler, S. M. & Sellers, J. R. Kinetic Adaptations of Myosins for Their Diverse Cellular Functions. *Traffic* **17**, 839-859, doi:10.1111/tra.12388 (2016).

30 Diz-Munoz, A., Fletcher, D. A. & Weiner, O. D. Use the force: membrane tension as an organizer of cell shape and motility. *Trends Cell Biol* **23**, 47-53, doi:10.1016/j.tcb.2012.09.006 (2013).

31 Butler, L. C. *et al.* Cell shape changes indicate a role for extrinsic tensile forces in Drosophila germ-band extension. *Nat Cell Biol* **11**, 859-864, doi:10.1038/ncb1894 (2009).

32 Lye, C. M. *et al.* Mechanical Coupling between Endoderm Invagination and Axis Extension in Drosophila. *PLoS Biol* **13**, e1002292, doi:10.1371/journal.pbio.1002292 (2015).

33 Morize, P., Christiansen, A. E., Costa, M., Parks, S. & Wieschaus, E. Hyperactivation of the folded gastrulation pathway induces specific cell shape changes. *Development* **125**, 589-597 (1998).

34 Huang, J., Zhou, W., Dong, W., Watson, A. M. & Hong, Y. From the Cover: Directed, efficient, and versatile modifications of the Drosophila genome by genomic engineering. *Proc Natl Acad Sci U S A* **106**, 8284-8289, doi:10.1073/pnas.0900641106 (2009).

35 Rauzi, M., Lenne, P. F. & Lecuit, T. Planar polarized actomyosin contractile flows control epithelial junction remodelling. *Nature* **468**, 1110-1114, doi:10.1038/nature09566 (2010).

36 Venken, K. J. *et al.* Versatile P[acman] BAC libraries for transgenesis studies in Drosophila melanogaster. *Nat Methods* **6**, 431-434, doi:10.1038/nmeth.1331 (2009).

37 Bertet, C., Sulak, L. & Lecuit, T. Myosin-dependent junction remodelling controls planar cell intercalation and axis elongation. *Nature* **429**, 667-671, doi:10.1038/nature02590 (2004).

38 Cavey, M. & Lecuit, T. Imaging cellular and molecular dynamics in live embryos using fluorescent proteins. *Methods Mol Biol* **420**, 219-238, doi:10.1007/978-1-59745-583-1_13 (2008).

39 Muller, H. A. Immunolabeling of embryos. *Methods Mol Biol* **420**, 207-218, doi:10.1007/978-1-59745-583-1_12 (2008).

40 Fuse, N., Yu, F. & Hirose, S. Gprk2 adjusts Fog signaling to organize cell movements in Drosophila gastrulation. *Development* **140**, 4246-4255, doi:10.1242/dev.093625 (2013).

41 Kosman, D., Small, S. & Reinitz, J. Rapid preparation of a panel of polyclonal antibodies to

Drosophila segmentation proteins. *Dev Genes Evol* **208**, 290-294 (1998).

42 Aigouy, B. *et al.* Cell flow reorients the axis of planar polarity in the wing epithelium of Drosophila. *Cell* **142**, 773-786, doi:10.1016/j.cell.2010.07.042 (2010).

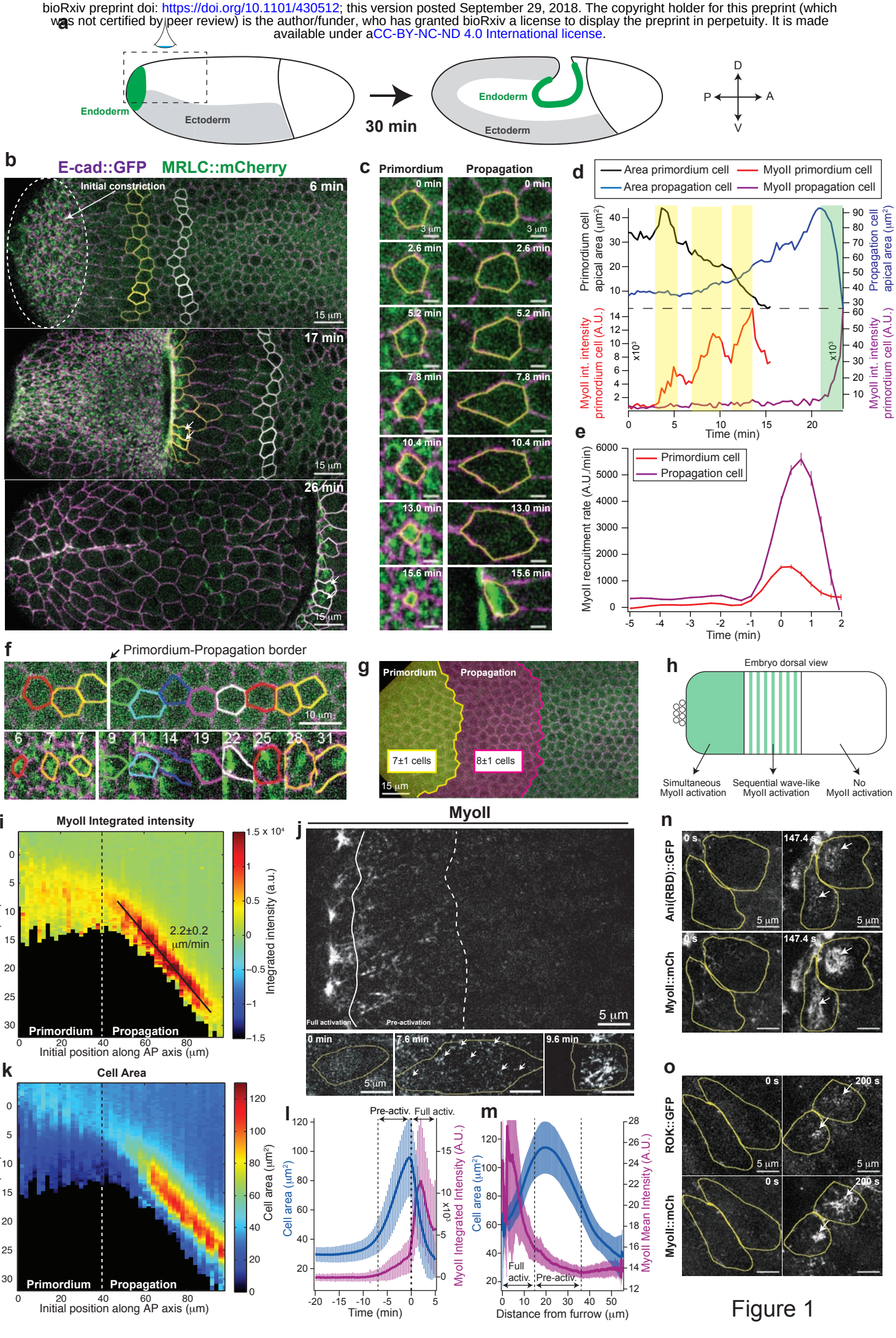


Figure 1

**Figure 1. Propagation of MyoII and Rho1 activation during morphogenesis of the posterior endoderm :** (**a**) Cartoon of endoderm morphogenesis during embryonic axis extension. On the left: the ventrolateral ectoderm (in grey) and the posterior endoderm (in green) are depicted at the onset of axis extension and 30' later. The dotted box indicates the region of imaging. (**b**) Time-lapse confocal images of endoderm morphogenesis. The dashed oval marks the primordium region and yellow and white contours mark cells of the propagation region where MyoII is activated at 17min and at 26min, respectively (indicated by arrows). (**c**) Close up views of a cell in the primordium (left) and propagation (right) regions. (**d**) Measurements of apical cell area and MyoII integrated intensity of the cells in **c**. (**e**) Measurements of MyoII recruitment rate in cells of the primordium and propagation region (N=288 cells for the primordium and 456 cells for the propagation region from 6 embryos). Time 0 is defined for each cell when MyoII intensity reaches a threshold (see methods). (**f**) Top: A row of endoderm cells aligned along the AP-axis across the primordium and propagation regions. Bottom: Collage of the frames of MyoII activation of the cells in the top image. Time of activation is indicated in minutes. Note the similar times of activation in the primordium and sequential activation in the propagation zone. (**g**) The primordium and the propagation region mapped on the dorsal epithelium at onset of gastrulation. (**h**) A cartoon summarizing the different MyoII activation behaviors in different regions of the dorsal epithelium. (**i-k**) Kymograph heat-maps of MyoII integrated intensity (**i**) and apical cell area (**k**) obtained from cell tracking in the endoderm. The dashed line indicates the primordium and propagation regions and the black solid line indicates the constant travelling speed of the MyoII wave. N=947 cells from 5 embryos. (**j**) High resolution images of MyoII recruitment in cells of the propagation region. Top: a larger view on the propagation zone from the invaginating furrow towards the anterior. The solid line denotes the region where cells reach high MyoII activation and the dashed line the region of low level MyoII recruitment (pre-activation). Bottom: stills from a single cell. White arrows indicate MyoII speckles denoting pre-activation. The yellow line indicates the cell contour. (**l**) Average time course of apical cell area and MyoII integrated intensity in cells in the propagation zone (N=456 cells from 6 embryos). Time 0 is defined as in **e**; full activation and pre-activation are indicated. (**m**) Space-intensity plot (see methods) of MyoII and cell apical area in the propagation region. The regions of full activation and pre-activation are indicated. N=6 embryos. (**n-o**) High resolution stills of cells in the propagation region labeled with MyoII and with the Rho1-GTP sensor, Anillin(RBD)::GFP (**n**), and RokKD::GFP (**o**) with the yellow line indicating cell contours.
In **b**, **d**, **f**, **i**, **k**, time T0=0 min is the onset of endoderm morphogenesis (see methods). Mean ± s.e.m. are shown in **e** and mean ± SD are shown in **l** and **m**.

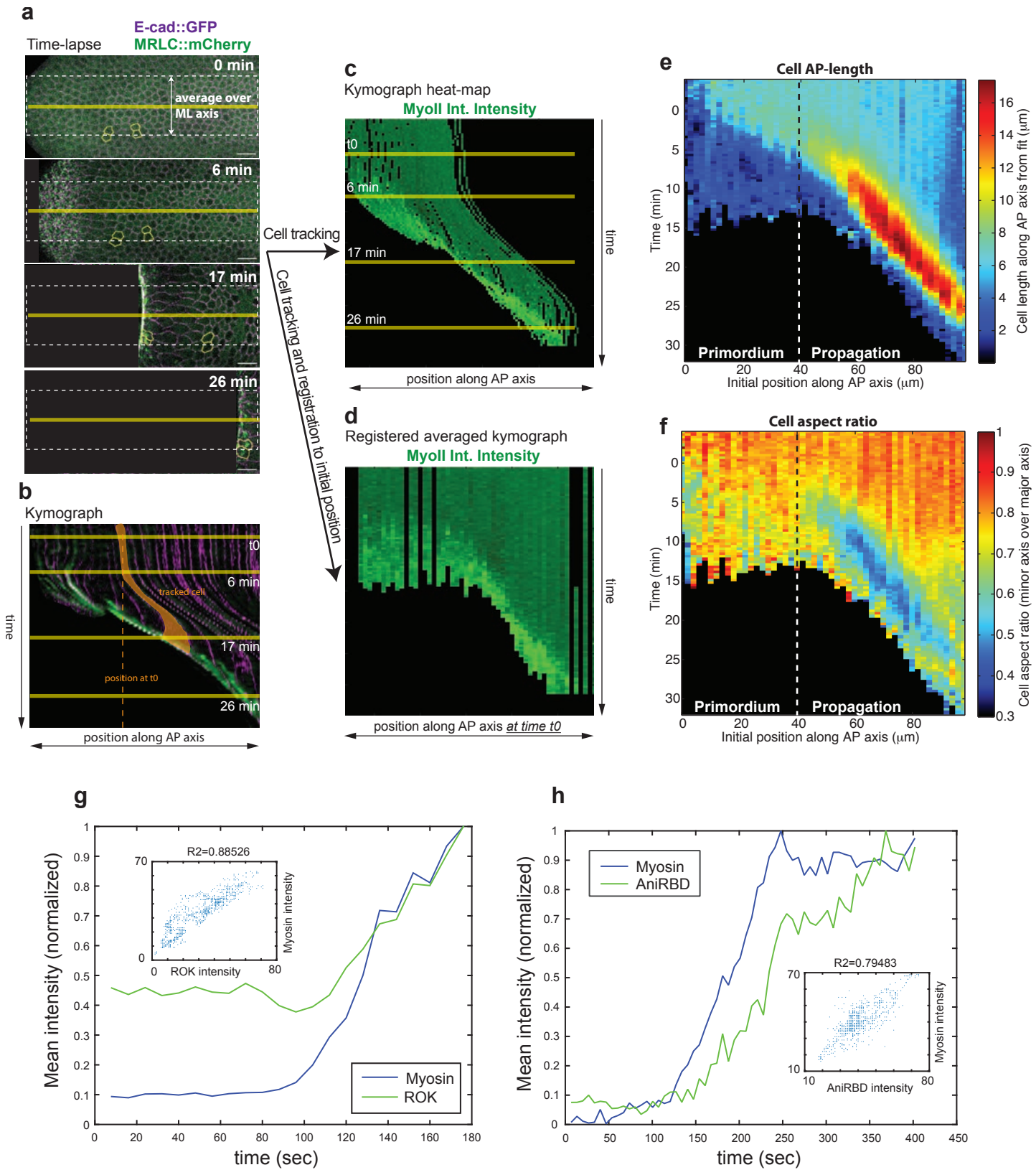


Ext. Fig. 1

**Extended Figure 1. Quantifications of MyoII and Rho1 propagation within the dorsal posterior epithelium (related to Fig.1):** (**a-d**) Procedure to generate kymograph heat-maps from time-lapses of endoderm morphogenesis. In **a** stills of a dual color time-lapse, E-cad::GFP is used to label cell contours and MyoII is labeled with mCherry. Cell tracking is performed (few tracked cells are displayed in yellow) and cell positions and MyoII intensities are extracted over time. (**b**) A kymograph generated along the yellow horizontal line in **a**. A single cell, highlighted in yellow, first moves with the tissue towards the anterior and then increases its apical area before recruiting MyoII. Solid yellow lines indicate the time frames in **a** and the dashed vertical line the position of the cell at time t0. (**c**) Kymograph heat-map of MyoII integrated intensity extracted from cell tracking in **a**. Data are averaged along the ML (here shown for a single embryo) axis within the white dashed line box in **a** and cell positions are the positions at time t. Note that some visible individual cell tracks display movements similar to the kymograph in **b**. (**d**) Kymograph heat-map of MyoII integrated intensity registered on the cell positions at time t0 extracted from cell tracking in **a**. Data are averaged along the ML axis (here shown for a single embryo), as in **c**, but now each cell track is plotted according to its position along the AP axis at time t0. Note that some visible individual cell tracks do not display any movement and appear as straight vertical lines. As a result tissue deformation is not considered and the movement of the wave across the tissue can be visualized. This representation is used throughout in this manuscript. Time t0 is the onset of endoderm morphogenesis. (**e-f**) Kymograph heat-maps of AP cell length (**e**) and cell aspect ratio (**k**). The primordium and propagation regions are indicated. N=947 cells from 5 embryos. (**g-h**) Representative examples curves of MyoII and Rok (**g**) or Rho1 sensor (**h**) mean intensity over time in one cell of the propagation region. Intensity values are normalized to the max of each curve for visualization purposes. In the insets, scatter plots of MyoII intensity vs Rok intensity (**g**) or Rho1 sensor intensity (**h)** from ~7 cells of the embryo shown in Fig.1**n** and ~10 cells of the embryo shown in Fig.1**o** (see methods).

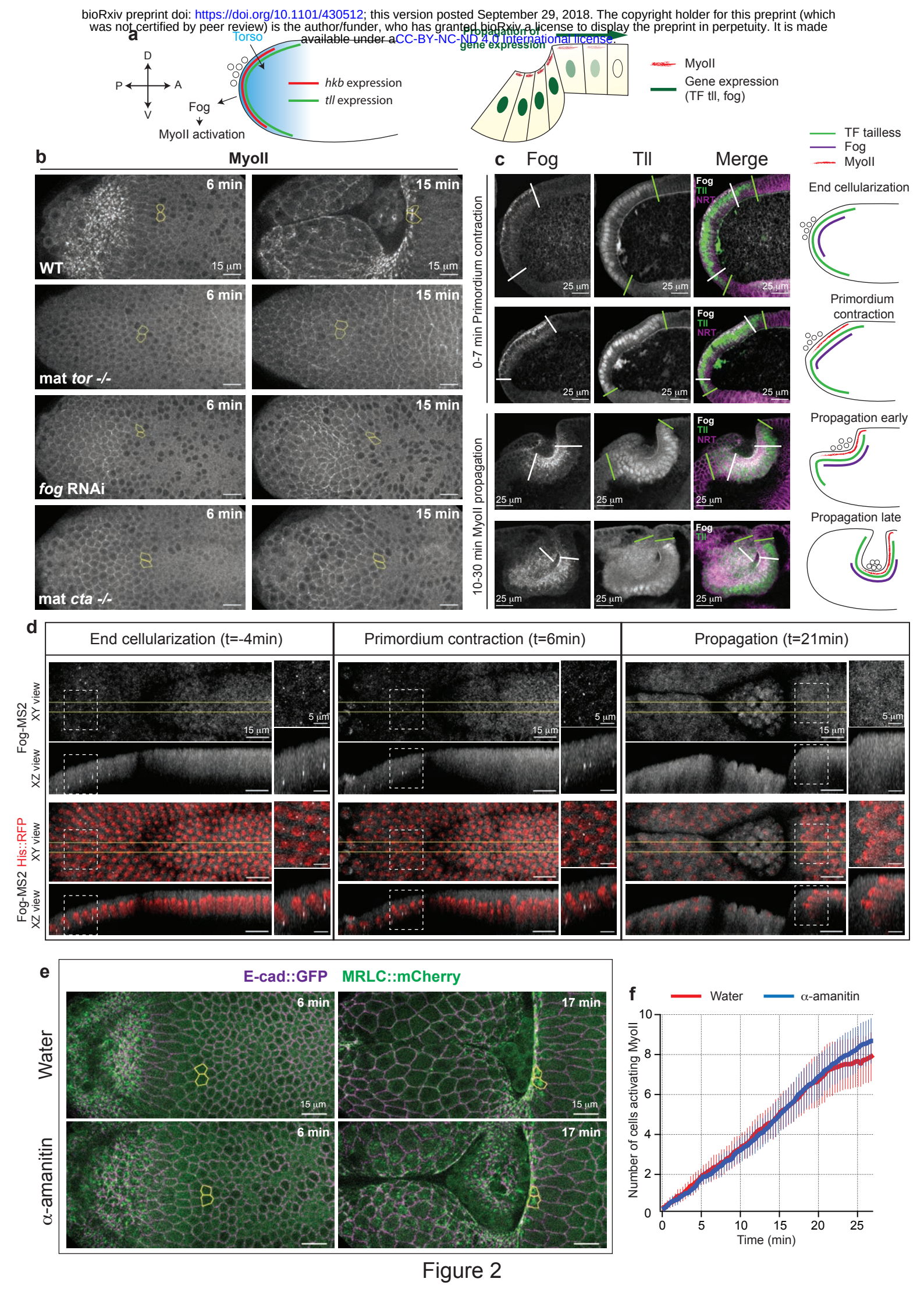


Figure 2

**Figure 2 MyoII activation in the primordium but not in the propagation region is controlled by gene transcription:** (**a**) Left: schematics of the terminal patterning-dependent pathway controlling MyoII activation in the posterior endoderm. Right: Cartoon of the dorsal epithelium in sagittal section describing the hypothesis of spatio-temporal changes in gene expression controlling MyoII propagation. (**b**) MyoII activation in the posterior endoderm in embryos mutant for torso (mat *tor*-/-), depleted of maternal and zygotic *fog* (*fog* RNAi) and mutant for the Gα12/13 Concertina (mat *cta*-/-). Yellow contours mark cells in the propagation region. (**c**) Sagittal sections of embryos immunostained for Fog and Tll (together with the membrane marker Neurotactin in the merge) at different stages of posterior endoderm morphogenesis. On the right a cartoon representation of the distribution of the indicated molecules. (**d**) *fog* expression in the posterior endoderm visualized with the MS2-MCP system[16] in living embryos. Top and side views of MCP::GFP and merge with Histone::RFP labelling nuclei are shown for the indicated time points. White dashed boxes indicate the positions of the close-ups on the right and the yellow lines the region where side-views were generated. (**e**) Posterior endoderm morphogenesis in water and α-amanitin injected embryos. Yellow contours mark cells in the propagation region. (**f**) Quantifications of the MyoII activation wave in water and α-amanitin injected embryos. The number of cells aligned along the AP-axis activating MyoII in the propagation region over time was measured. N=11 for water and N=10 for α-amanitin injected embryos. Mean ± SD are shown.

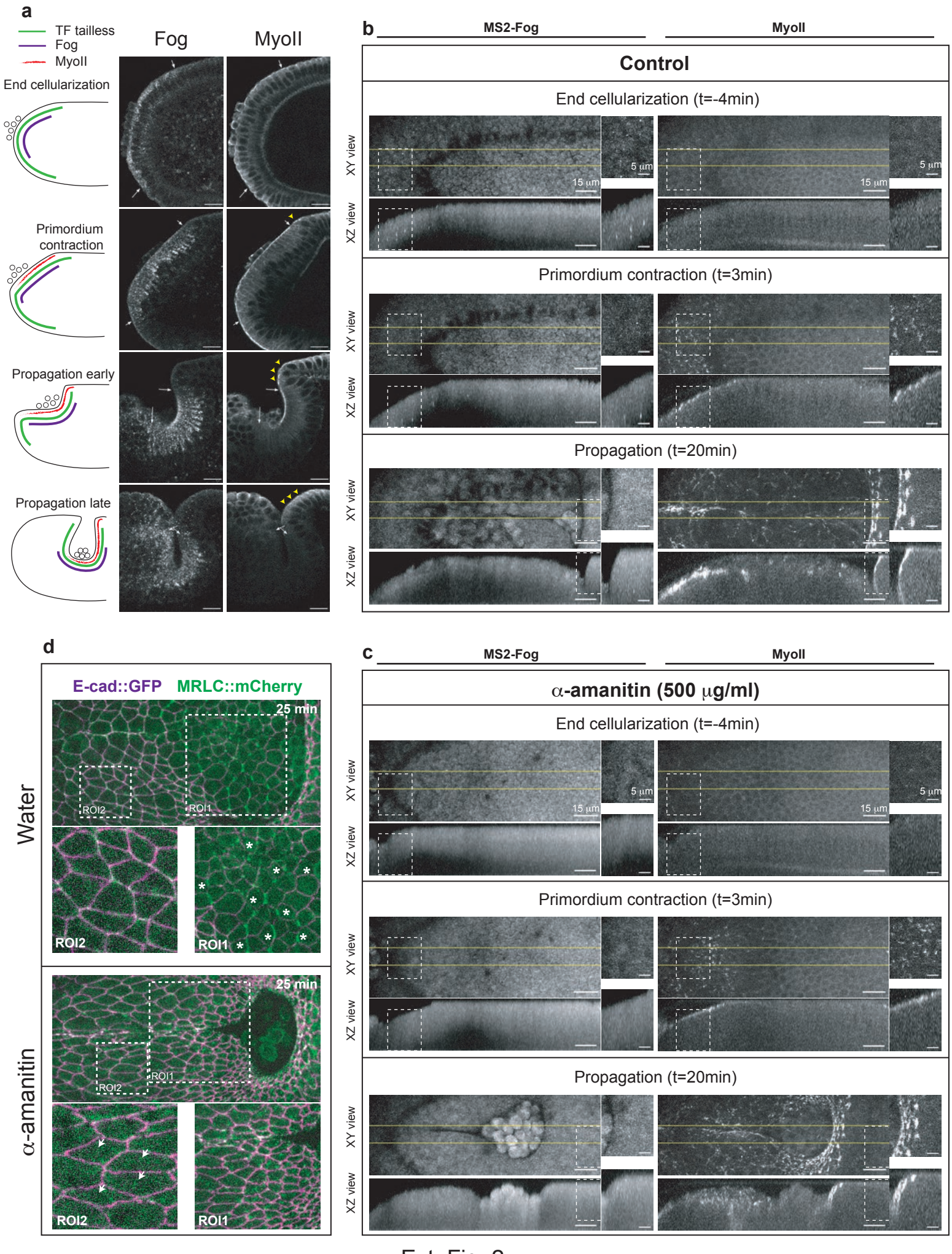


Ext. Fig. 2

**Extended Figure 2 MyoII propagation is not controlled transcriptionally (related to Fig.2):** (**a**) Sagittal sections of embryos stained for Fog and MyoII at different stages of posterior endoderm morphogenesis. On the left a cartoon representation of the distribution of the indicated molecules. (**b-c**) *fog* expression and MyoII recruitment in control (**b**) and α-amanitin injected (**c**) living embryos. Top and side views are shown for the indicated time points. White dashed boxes indicate the positions of the close-ups on the right and the yellow lines the region where side-views were generated. In control embryos *fog* is expressed in the primordium but not in the propagation zone. Note that in α-amanitin injected embryos *fog* expression is lost very rapidly in the primordium after injection (absence of MCP-labelled bright dots). (**d**) Stills of a water and α-amanitin injected embryo at a late stage of invagination. Asterisks indicate dividing cells (ROI1) and arrowheads elongated cells in the posterior-ventrolateral ectoderm. Elongated cells in the ectoderm are a hallmark of cell stretching typical of conditions where cell intercalation is affected[23,31,32].

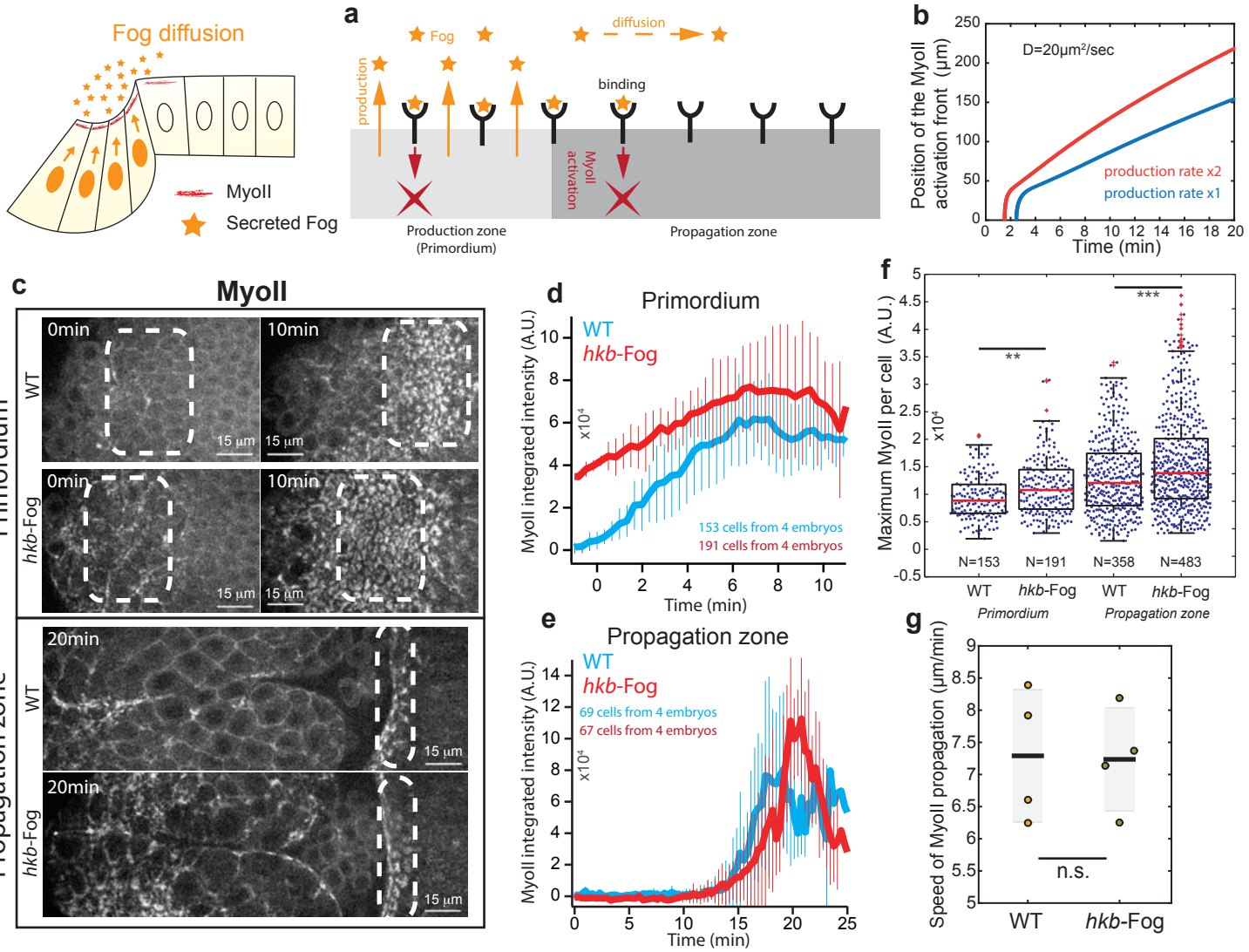


Figure 3

**Figure 3 Diffusion or transport of secreted Fog does not control MyoII wave propagation:** Top left: Cartoon describing the hypothesis of secreted Fog diffusion or transport from the primordium controlling MyoII propagation. (**a**) Schematic representation of the model of Fog secretion, diffusion, receptor binding and MyoII activation (see details in Supplementary Methods). (**b**) Position of MyoII activation front over time obtained from simulations using the model described in **a** for the indicated diffusion constant (D), a given production rate (blue) and twice this rate (red). (**c**) Time-lapse of MyoII recruitment in the primordium and propagation region of WT and embryos overexpressing Fog in the primordium (hkb-*fog*). The dashed line boxes mark the primordium and the activated cells in the propagation region respectively. (**d-e**) Time course of MyoII integrated intensity in cells of the primordium (**d,** N=153 and 191 cells for WT and hkb-*fog* from 4 embryos each) and in a 10 µm band of cells at ~30 µm distance from the primordium at time t0 (**e,** N=69 and 67 cells for WT and hkb-*fog* from 4 embryos each). Mean ± SD between different embryos are shown. (**f**) Maximum of MyoII integrated intensity in cells of the indicated conditions. Box plots are superimposed to individual data points. N indicates the number of cells from 4 embryos for each condition. ** indicates a P<0.01 and *** a P<0.001 from a Mann-Whitney test. (**g**) Speed of the MyoII propagation front in the reference frame of the embryo (see methods). Individual data points are superimposed to box plots (dark line: mean, light grey zone: 95% s.e.m., darker grey zone: s.d.). N=4 embryos each. N.S. indicates a P>0.05 from a Mann-Whitney test. (**h**) MyoII pattern in an embryo where Fog (left), a constitutively active form of Gα12/13 (middle) or a constitutively active form of Rho1 (right) are expressed uniformly (using 67-Gal4). The yellow and orange lines denote the limits of the primordium and propagation regions respectively. (**i**) Left: Pathway of MyoII activation by Fog in endoderm cells. Right: Schematic of WT and uniform expression of Fog in the embryo. Fog expression pattern is shown in orange and the resulting MyoII pattern in green. The MyoII active and inactive zones used to calculate the MyoII tissue level gradients in **j** are indicated. (**j-k**) Quantifications of MyoII tissue-level polarity (**j**) and of the number of cells activating MyoII in the propagation region in embryos of the indicated conditions (**k**). Individual data points are superimposed to box plots (dark line: mean, light grey zone: 95% s.e.m., darker grey zone: s.d.). N indicates the number of embryos. For **j**, ** indicates a P<0.01 and *** a P<0.001 at a one-sample Student test. For **k**, N.S. indicates a P>0.05 and ** a P<0.01 from a Mann-Whitney test.

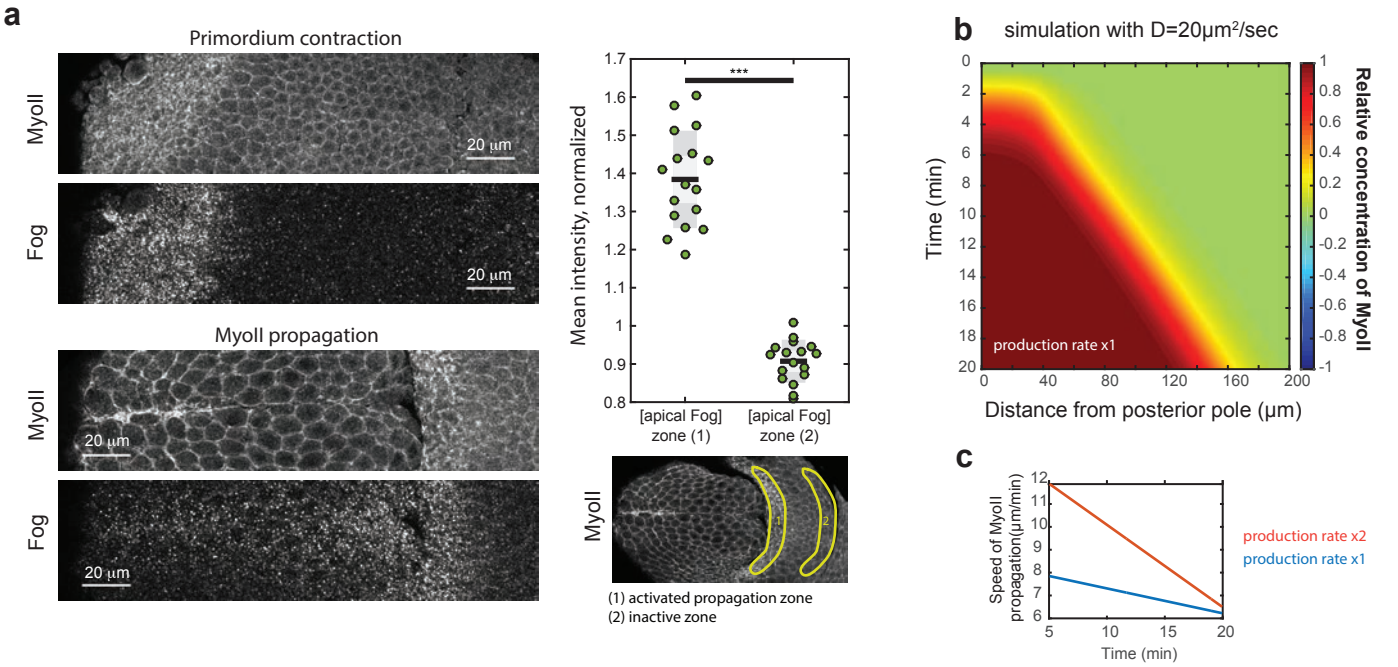


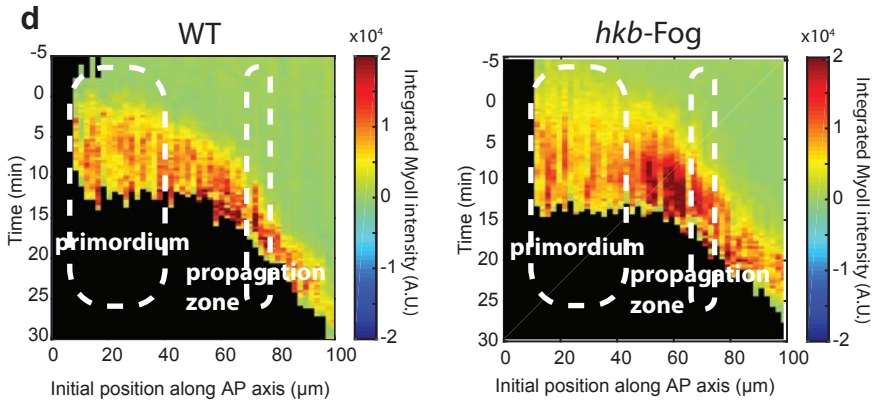


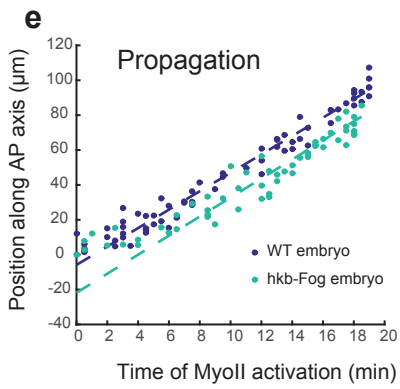


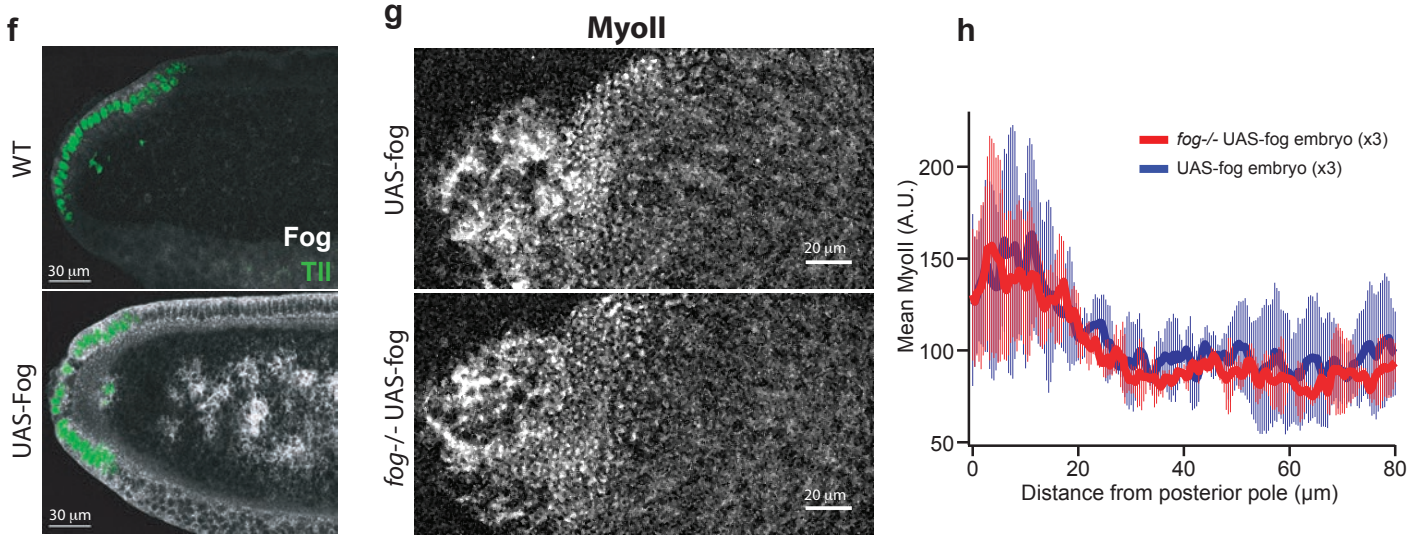


Ext. Fig. 3

**Extended Figure 3 Diffusion or transport of secreted Fog does not control MyoII wave propagation (related to Fig.3):** (**a**) Left: Apical sections of embryos stained for Fog and MyoII at primordium contraction and late propagation stages during endoderm morphogenesis. Right: Quantifications of Fog mean intensity in the indicated active and inactive zones in the propagation region. Individual embryos data points are superimposed to box plots (dark line: mean, light grey zone: 95% s.e.m., darker grey zone: s.d.). **** indicates a P<0.0001 from a Mann-Whitney test. (**b**) Kymograph heat-map of MyoII concentration from a simulation of the model introduced in Fig.3a. (**c**) Speed of MyoII propagation over time in the indicated conditions as measured from simulations of the model in Fig.3a. (**d**) Kymograph heat-maps of MyoII integrated intensity for the indicated conditions. N=323 cells from 2 WT embryos and 853 cells from 4 *hkb*-Fog embryos. The white dashed boxes indicate the primordium region and the band of cells in the propagation zone used for the quantifications in Fig.3d-e. (**e**) Position of the MyoII activation front over time in the propagation zone for a representative WT and a *hkb*-Fog embryo. Dashed lines are linear fits of the cell positions at the time of MyoII activation in the embryo reference frame (see methods) as a function of their time of activation. (**f**) Sagittal sections of a WT and an embryo ubiquitously expressing Fog (UAS-Fog). Immunolabelling for Fog is shown in white and for Tailless (Tll) in green. (**g**) MyoII pattern in conditions of Fog ubiquitous expression in the background of WT and zygotic *fog* loss of function (imaged with 20X objective) (**h**) Quantifications of MyoII patterns along the AP-axis in the posterior endoderm of the indicated conditions. N=3 embryos each.

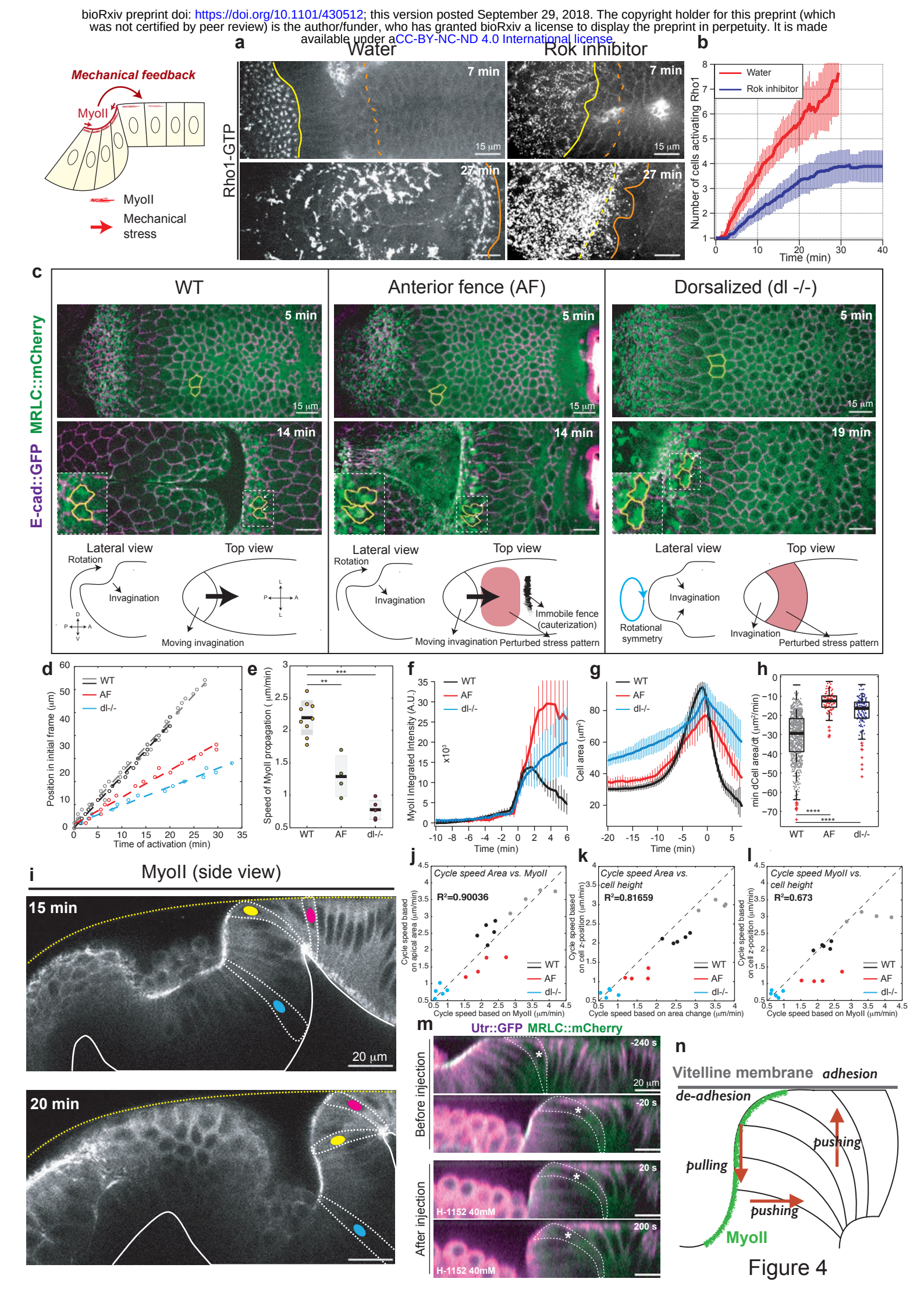


Figure 4

**Figure 4 The wave of MyoII is mechanically regulated and induces a 3D cycle of cell deformations:** Top left: Cartoon describing the hypothesis of a mechanical feedback controlling MyoII propagation. (**a**) Time-lapse stills of Anillin(RBD) (Rho1-GTP sensor) in water and H-1152 (Rok inhibitor) injected embryos. Embryos were injected at end of cellularization. The yellow and orange lines denote the limits of the primordium and propagation regions, respectively. (**b**) Quantifications of the wave of Rho1 activation as in Fig. 2f. N=10 for water and N=12 for H-1152 injected embryos (**c**) Time-lapse stills of a WT (left), an embryo with an anterior medio-lateral fence (AF, middle) and a dorsalized embryo (dl-/-, right). MyoII ::mCherry and cell contours labeled with Ecad::GFP are shown. Marked in yellow are representative tracked cells in the propagation region. Bottom: Schematic representations of the normal and perturbed conditions. (**d**) Position of the MyoII activation front over time in the propagation zone in the reference frame of the tissue. The dashed lines represent linear fits of cell position at the time of MyoII activation in the reference frame of the tissue (see methods) as a function of their time of activation. WT shown in grey and black are the controls for AF and dl-/- embryos, respectively. Grey WT and AF data have been scaled to match black WT controls. Unscaled data are shown in Extended Fig. 4d. (**e**) Speed of MyoII propagation in the reference frame of the tissue from data in **d**. Individual data points are superimposed to box plots (dark line: mean, light grey zone: 95% s.e.m., darker grey zone: s.d.). N=9 WT embryos, 4 AF embryos and 5 dl-/- embryos. ** indicates a $P<0.01$ and *** a $P<0.001$ from a Mann-Whitney test. (**f-g**) Time course of MyoII integrated intensity (**f**) and apical cell surface (**g**) of cells in the propagation region of embryos of the indicated conditions. Time 0 is defined for each cell as the point when MyoII intensity reaches a defined threshold (see methods). N=807 cells from 9 WT embryos, 87 cells from 4 AF embryos and 190 cells from 5 dl-/- embryos. (**h**) Minimum rate of apical constriction in cells of the propagation region for the indicated conditions. Box plots superimposed to individual data points. N=663 cells from 9 WT embryos, 93 cells from 4 AF embryos and 129 cells from 5 dl-/- embryos. **** indicates a $P<0.0001$ from a Mann-Whitney test. (**i**) Side views of MyoII recruitment and cell deformations in the propagation zone during posterior endoderm morphogenesis. Sagittal confocal sections were collected on a 2-photon microscope. The dashed white lines highlight cell contours, the yellow dashed line the vitelline membrane and the solid white line the basal side of the blastoderm epithelium. (**j-l**) Scatter plots of the speed of the mechanical cycle calculated from the MyoII activation front, the apical cell area and cell position along the apico-basal axis of the tissue for the indicated conditions. $R^2$ values for a fit y=x are shown. (**m**) Live injection of H-1152 (Rok inhibitor) during MyoII propagation. Reconstructed side views from confocal stacks are shown. White asterisks and dashed lines mark a single cell over time. T0 is the time of injection. (**n**) Schematic of the 3D mechanical cycle shown from the side as in **i**. In **a**, **c** and **i** T0 is the onset of endoderm morphogenesis. In **b**, **f**, and **g** mean ± SD between embryos are shown.

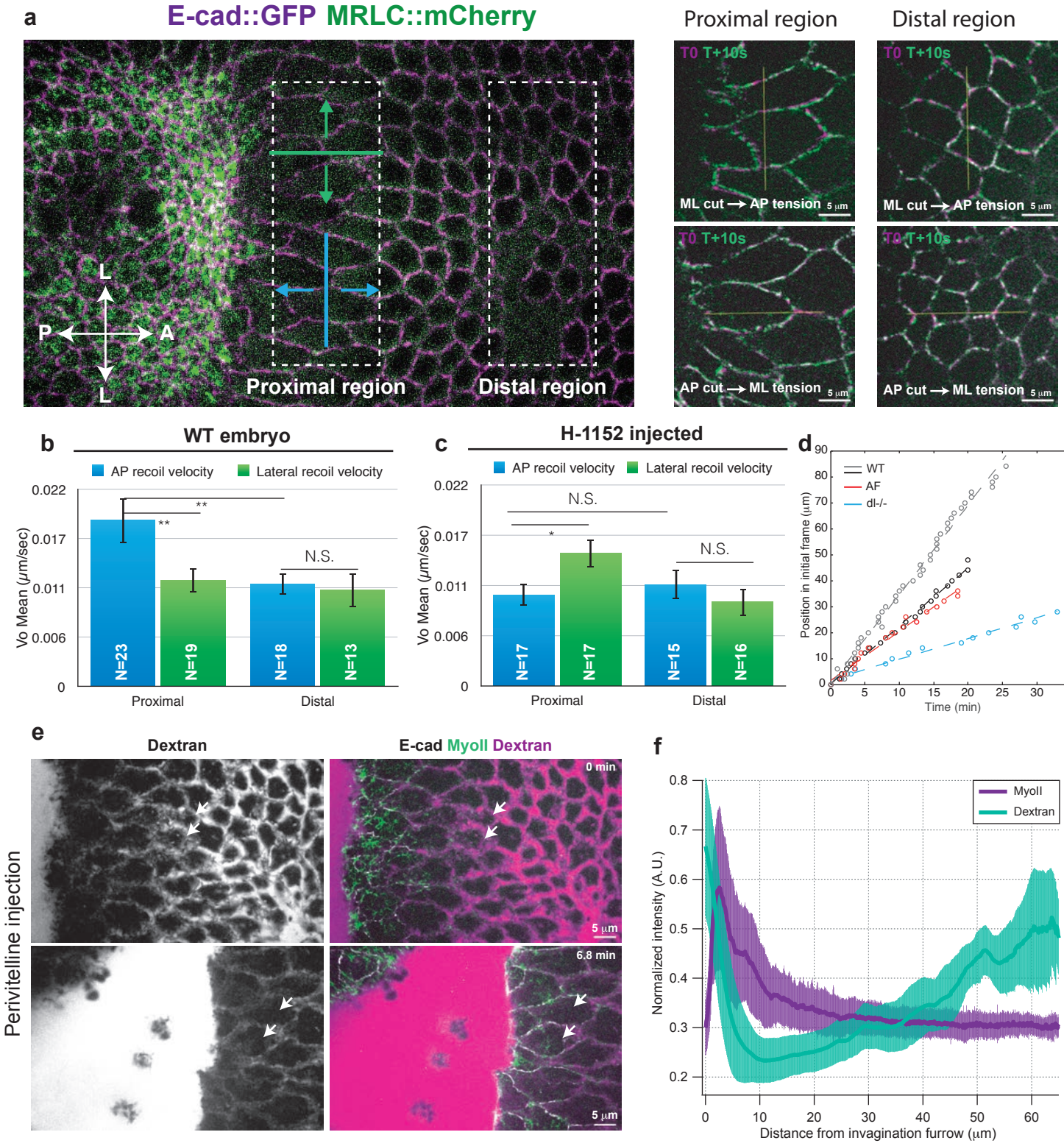


Ext. Fig. 4

**Extended Fig. 4 Cells in the propagation region are subjected to mechanical stresses (related to Fig.4):** (**a**) Left: Regions in the dorsal epithelium (corresponding to the propagation region) where tension was probed by line cuts with different orientations (ML cut in blue and AP cut in green). Right: Examples of ML and AP line cuts in the indicated regions. Overlays of the pre-cut (in magenta) and an image 10 s post-cut (in green) are shown. The yellow line indicates the line cut. (**b-c**) Quantifications of the tissue initial recoil velocity in the regions and line orientations illustrated in WT (**b**) and H-1152 (Rok inhibitor) injected embryos (**c**). N indicates the number of independent ablations extracted from 11 and 7 embryos for WT and H-1152 respectively. Mean values ± s.e.m. are shown. (**d**) Position of the MyoII activation front over time in the propagation zone in the reference frame of the tissue (unscaled data) as in Fig.4d. (**e**) Stills from a high-resolution time-laspe of dextran injection in the perivitelline space. Dextran alone is on the left and merge images with Ecad and MyoII on the right. Arrows indicate two cells as the invaginating furrows approaches. (**f**) Space-intensity plot of MyoII and dextran intensity in the propagation region. N=3 embryos. (**g**) Stills from a high-resolution time-lapse of MyoII and a plasma membrane marker (Gap-43) in cells of the dorsal epithelium during MyoII propagation. The white arrows indicate events of cell attachment to vitelline membrane.

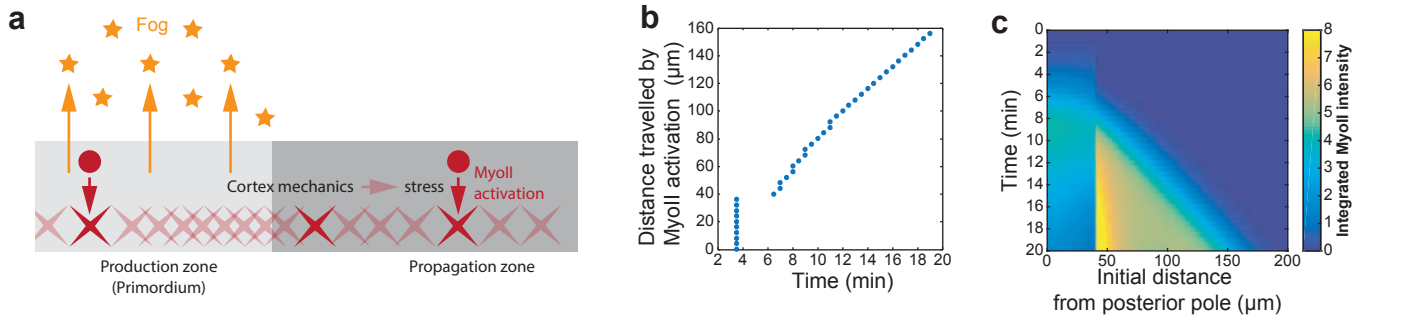


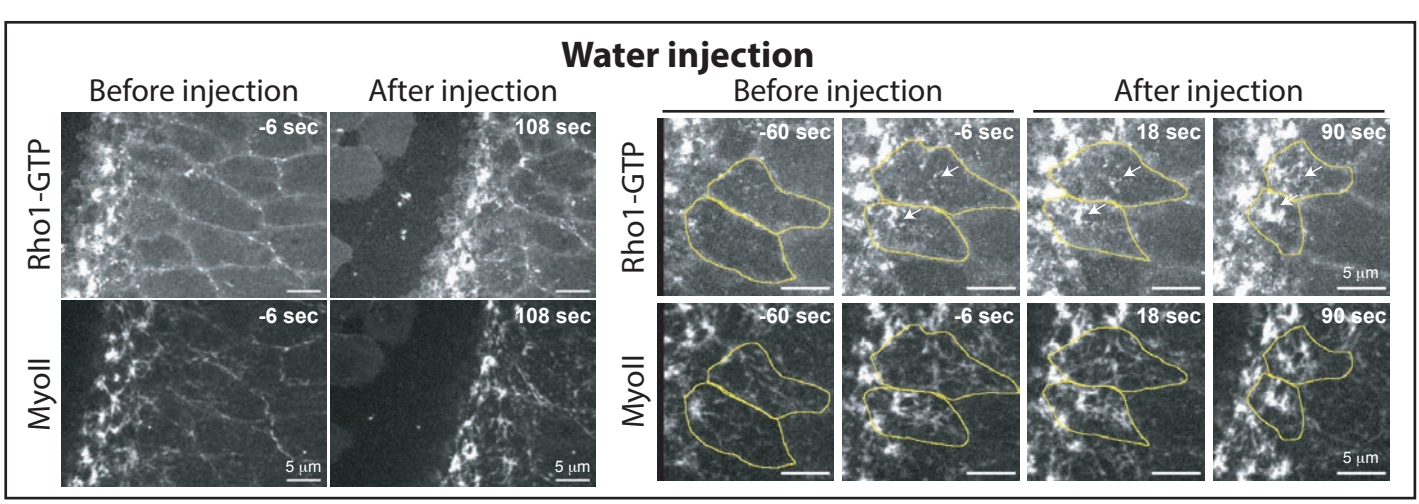


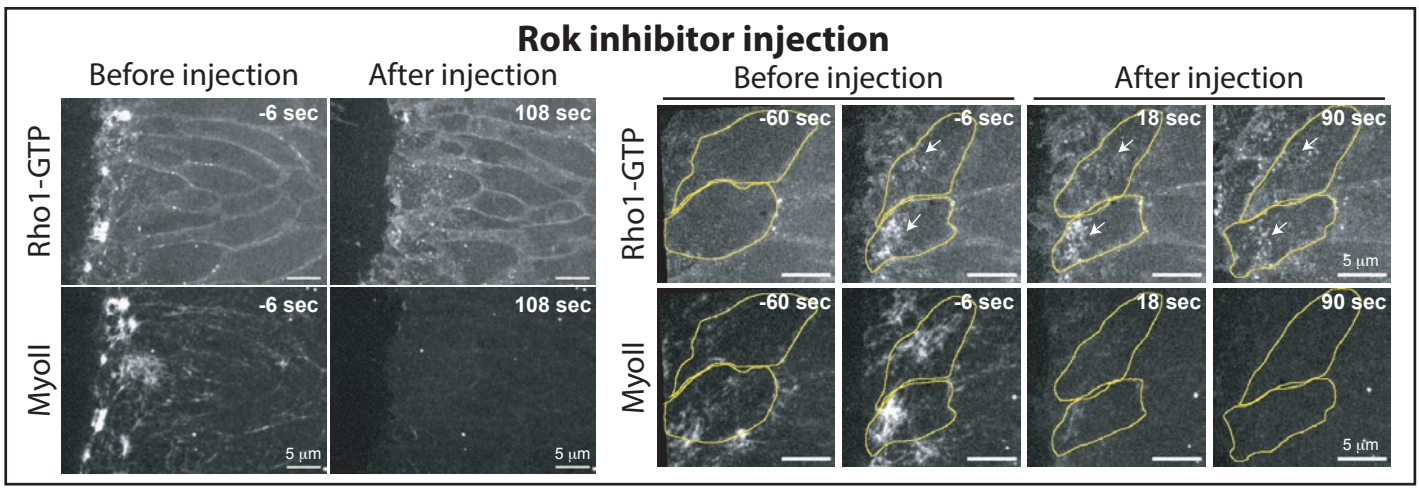


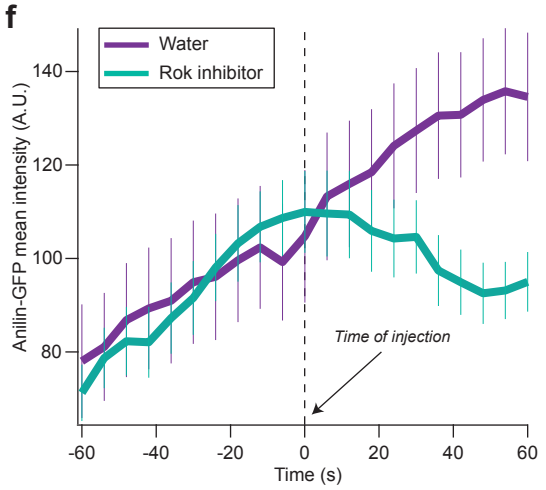


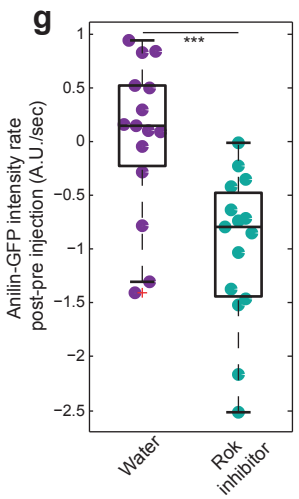


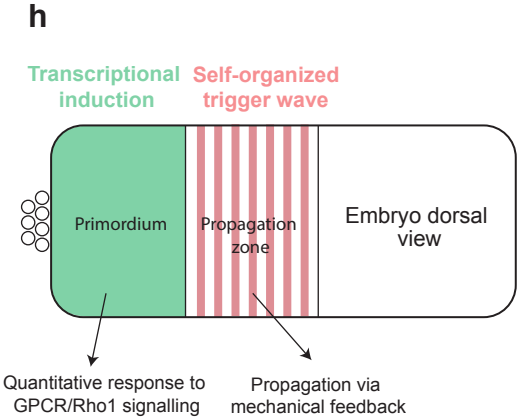


Figure 5

**Figure 5 Stress-based feedback on MyoII generates trigger waves and stabilizes Rho1 activation in cells:** (**a**) Schematic representation of the model used to study the effects a stress-based feedback on MyoII (see details in Supplementary Methods). Fog is produced in the primordium where it activates MyoII but it is not allowed to diffuse. (**b-c**) Position of MyoII activation front over time and activated MyoII quantity over space and time (represented in the form of a registered kymograph heat-map and equivalent to integrated MyoII intensity measured from time lapses) from simulations of the model in **a.** (**d-e**) Stills from high resolution time lapses of Rho1 sensor (Anillin(RBD)::GFP) and MyoII in water and H-1152 (Rok inhibitor) injected embryos during propagation. On the left: stills just before and after injection. On the right: close-up views on two cells before and after injection. Cell contours are outlined in yellow and the white arrows mark accumulations of Rho1-GTP. (**f-g**) Quantifications of the mean intensity of Rho1 sensor before and after injections. In **f** average mean intensity measurements over time are shown and in **g** quantifications of the Anillin(RBD)::GFP recruitment rate difference (post–pre injection) following Rok inhibitor injection. N=15 cells from 3 embryos in both water and H-1152 injections. *** indicates a $P<0.001$ from a Mann-Whitney test. Mean SD are shown in **f** and box plots overlaid to individual data in **g**. (**h**) Cartoon model of MyoII induction and propagation during posterior endoderm morphogenesis in *Drosophila* embryos. MyoII recruitment and apical constriction are first induced in the primordium region by a transcriptional program under the control of terminal patterning genes and then propagates anteriorly in a self-organized process depending on mechanical feedback amplification and spatial coupling.

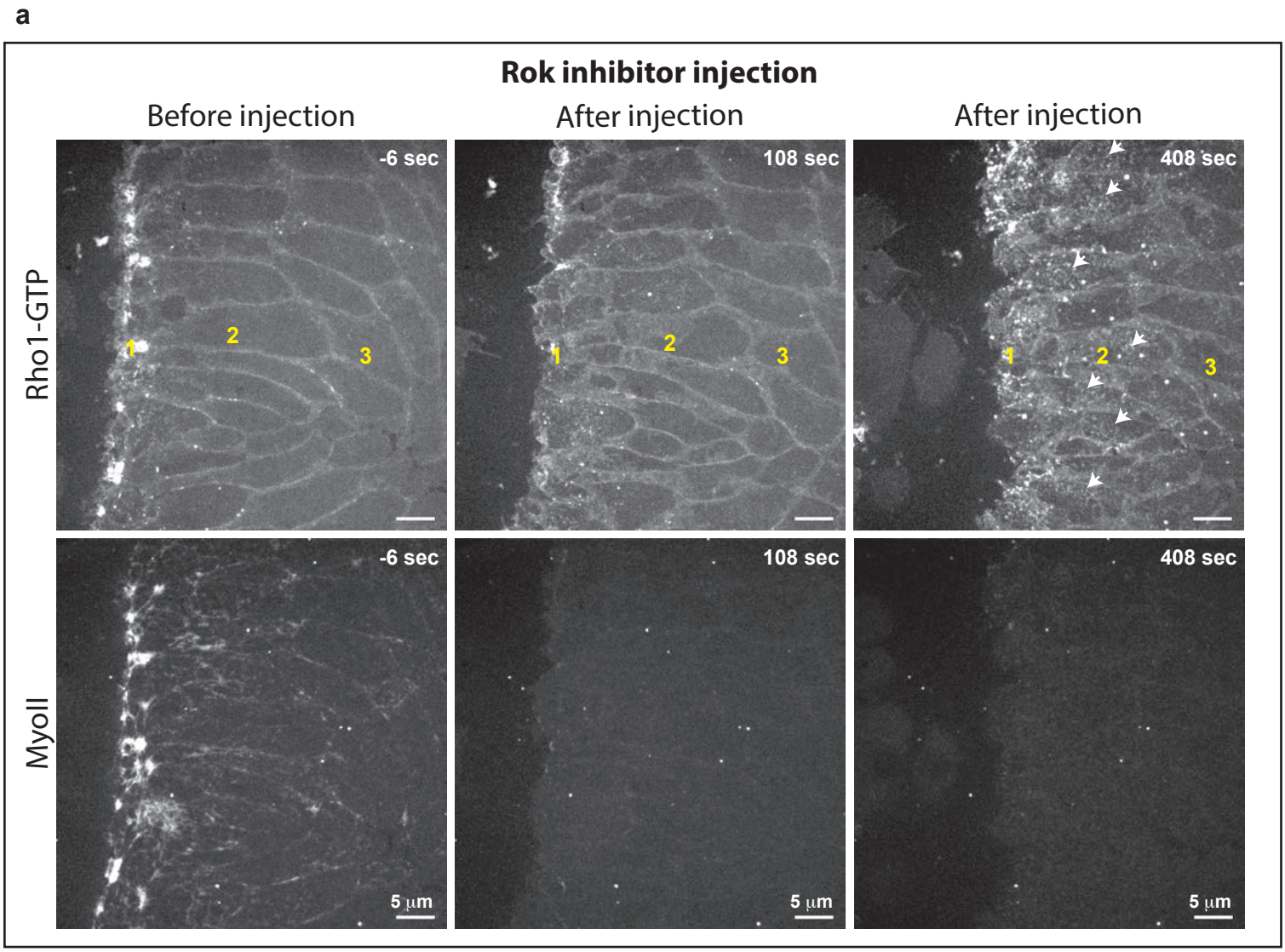


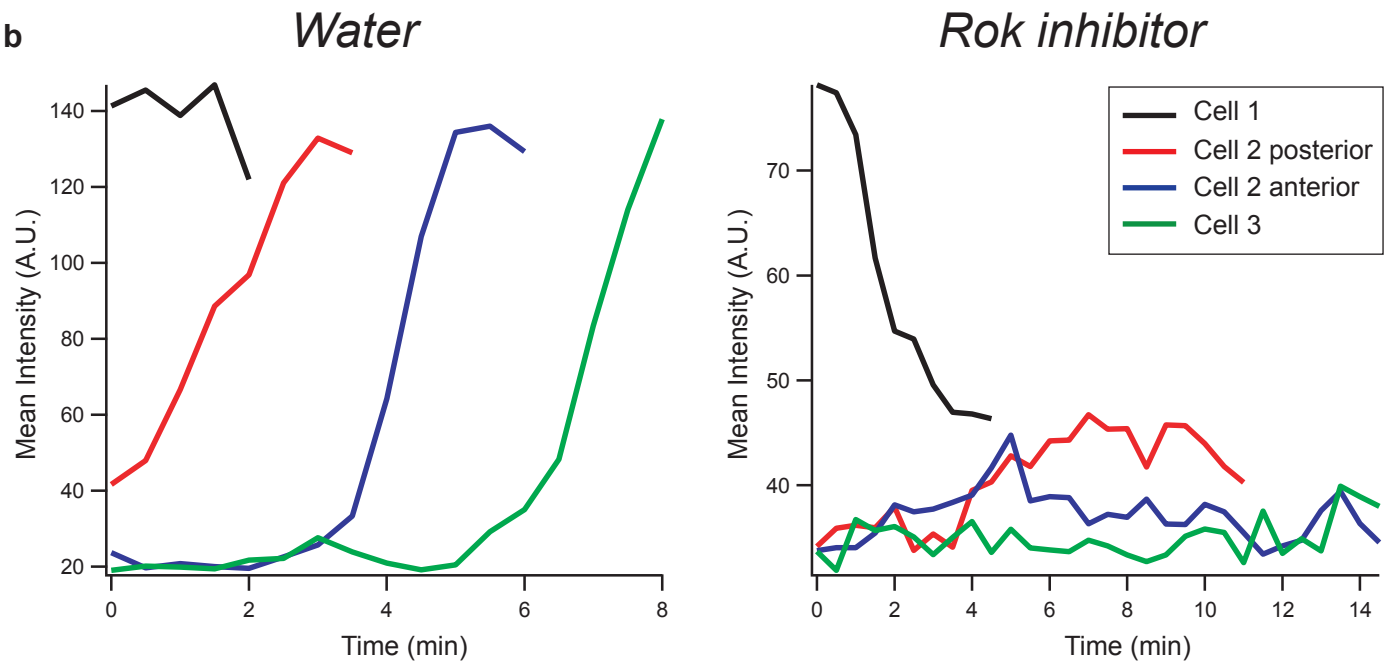


Ext. Fig. 5

**Extended Fig. 5 Rho1 activation in cells in the absence of mechanical feedback (related to Fig.5):** (**a**) Stills from a high resolution time lapse of Rho1 sensor (Anillin(RBD)::GFP) and MyoII in an embryo injected with 40 mM H-1152 (Rok inhibitor) during propagation. Later times after injection are shown (compared to Fig.5c) where a low level Rho1 activation is visible (indicated by white arrows). The numbers in yellow indicate cells belonging to cell rows at different distances from the invaginating furrow. (**b**) Measurement of Rho1 sensor (Anillin(RBD)::GFP) mean intensity over time in representative examples of cells (or regions of cells) at different distances from the invaginating furrow in water (left) and H-1152 (right) injected embryos.

## Movie Legends

**Movie 1:** Time-lapse of posterior endoderm morphogenesis in a WT embryo. E-cad::GFP is in magenta and MRLC::mCherry in green. The yellow contours mark tracked cells in the propagation zone. Scalebar 15 μm.

**Movie 2:** High resolution time-lapse of MRLC::GFP recruitment in cells in the propagation zone during posterior endoderm morphogenesis. Note the high level of MyoII activation close to the invaginating furrow and the lower levels more anteriorly. Scalebar 5 μm.

**Movie 3:** High resolution time-lapse of cells in the propagation region labelled with the Rho1-GTP sensor Ani(RDB)::GFP (left) and MyoII (right). The white arrows point to Rho1-GTP and MyoII accumulations during wave propagation. Scalebar 5 μm.

**Movie 4:** High resolution time-lapse of cells in the propagation region labelled with Rok(KD)::GFP (left) and MyoII (right). The white arrows point to Rok and MyoII accumulations during wave propagation. Scalebar 5 μm.

**Movie 5:** Time-lapse of MyoII activation during posterior endoderm morphogenesis in a *torso* mutant embryo (laid by mothers *tor -/-,* top), in a strong knock-down of fog (fog RNAi, middle) and in a *concertina* (Gα12/13) mutant embryo (laid by mothers *cta -/-,* bottom). MyoII is labelled with MRLC::mCherry. Scalebar is 20 μm.

**Movie 6:** Top and side views of *fog* expression (MS2-*fog* revealed by MCP::GFP) on the left and MyoII (MRLC::mCherry) activation on the right during posterior endoderm morphogenesis in a WT embryo. Scalebar 15 μm.

**Movie 7:** Top and side views of *fog* expression (MS2-*fog* revealed by MCP::GFP) on the left and MyoII (MRLC::mCherry) activation on the right during posterior endoderm morphogenesis in a water (top) and α-amanitin (bottom) injected embryos. Scalebar 15 μm.

**Movie 8:** Time-lapse of MyoII activation and propagation during posterior endoderm morphogenesis in a water (top) and α-amanitin (bottom) injected embryos. E-cad::GFP is magenta and MRLC::mCherry in green. The yellow contours mark tracked cells in the propagation zone and the white arrows indicate cells at the moment of MyoII activation. Scalebar 20 μm.

**Movie 9:** Time-lapse of MyoII activation and propagation during posterior endoderm morphogenesis in a WT (top) and an embryo over-expressing *fog* in the primordium (hkb-Fog, bottom) injected embryos. E-cad::GFP is magenta and MRLC::mCherry in green. Time registration has been performed as described in the methods. Scalebar 20 μm.

**Movie 10:** Time-lapse of MyoII activation during posterior endoderm morphogenesis in embryos expressing ubiquitously *fog* (UAS-Fog, top), a constitutively active version of Gα12/13, (UAS-Cta[CA], middle) or a constitutively active version of Rho1 (UAS-Rho1[CA], bottom). MyoII is labelled with MRLC::mCherry. Scalebar 20 μm.

**Movie 11:** Rho1 and MyoII activation and propagation during posterior endoderm morphogenesis in a water injected embryo at end of cellularization. Rho1-GFP is detected with the Rho1 sensor Ani(RDB)::GFP (top) and MyoII is labelled with MRLC::mCherry (bottom). The white arrows indicate events of Rho1 and MyoII activation in cells of the propagation region. Scalebar 15 μm.

**Movie 12:** Rho1 and MyoII activation and propagation during posterior endoderm morphogenesis in an embryo injected with the Rok inhibitor H-1152 at the end of cellularization. Rho1-GFP is detected with the Rho1 sensor Ani(RDB)::GFP (top) and MyoII is labelled with MRLC::mCherry (bottom). The white arrows indicate events of Rho1 and MyoII activation in cells of the propagation region. Scalebar 15 μm.

**Movie 13:** Posterior endoderm morphogenesis in a WT embryo (top), an embryo with an anterior dorsal fence (middle) and a dorsalized embryo laid by *dorsal* -/- mothers (bottom). E-cad::GFP is in magenta and MRLC::mCherry in green. The yellow contours mark tracked cells in the propagation zone. Scalebar 15 μm.

**Movie 14:** Gastrulation in a WT (top) and a dorsalized embryo laid by *dorsal* -/- mothers (bottom). Scalebar 50 μm.

**Movie 15:** Side view of MyoII recruitment and cell deformations during posterior endoderm morphogenesis. MyoII is labelled MRLC::GFP and the white arrows indicate events of MyoII activation during wave propagation. Scalebar 20 μm.

**Movie 16:** Time-lapse of a Rok inhibitor (H-1152) injection during MyoII propagation. Top and side views are shown. F-actin, labelling cell contours, is detected with Utrophin(ADB)::GFP (top) and MyoII is labelled with MRLC::mCherry (bottom). The label H-1152 marks the time of injection. Scalebar 15 μm.

**Movie 17:** Time-lapse of cells in the propagation region illustrating events of transient cell adherence to the vitelline membrane (seen as cells lagging behind the moving invaginating furrow and then suddenly snapping down in the invagination). MyoII, labelled by MRLC::GFP, is in white and cell plasma membrane, labelled by Gap-43::mCherry, is in green. Scalebar 5 μm.

**Movie 18:** Time-lapse of a water (left) or Rok inhibitor (H-1152) injection during Rho1/MyoII wave propagation. Rho1-GFP is detected with the Rho1 sensor Ani(RDB)::GFP (top) and MyoII is labelled with MRLC::mCherry (bottom). Close-up on cells in the process of activating Rho1/MyoII at the time of injection. The white arrows point to Rho1-GTP and MyoII accumulations just before injection. The labels 'Water' and 'H-1152' mark the time of injection. Scalebar 5 μm.

**Movie 19:** Time-lapse of a water (left) or Rok inhibitor (H-1152) injection during Rho1/MyoII wave propagation. Rho1-GFP is detected with the Rho1 sensor Ani(RDB)::GFP (top) and MyoII is labelled with MRLC::mCherry (bottom). Larger views and longer time lapse after injection. Note the slow and low-level activation of Rho1 in cells anterior to the invaginating furrow following Rok inhibition (top right). Scalebar 5 μm.

# Materials and Methods

## Fly strains and genetics

The following mutant alleles and insertions were used: *tor*[4], *dl*[1], *fog*[4a6], *cta*[RC10], *sqh*[AX3], *pUAST-fog*[6] [13], *pUAST-ctaQ303L* [33], *UAS-rho1V14* (Bloomington stock #8144), *hkb-fog* (chromosome 3 from [20]). MyoII RLC (MRLC) is encoded by the gene *spaghetti-squash* (*sqh*, Genebank ID: AY122159). Live cell imaging of Sqh was carried out using *sqh-Sqh::mCherry* (on chromosome 2 from [8] and a new insertions at the VK18 site, located 53B2 on chromosome 2 or the VK27 site located 89E11 on chromosome 3), *sqh-Sqh::mKate2* (insertion at the VK27 site, located 89E11 on chromosome 3) and *sqh-Sqh::GFP* transgenics (gift from R. Karess). *E-Cad::EGFP* is a EGFP knock-in allele of E-Cadherin at the locus generated by homologous recombination (*E-cad::EGFP*[Kin], [34]). F-Actin was visualized using a *sqh-Utrophin::EGFP* insertion on chromosome 3 [35]. Live imaging of the Rho1 sensor and Rok were carried out using a *ubi-Anilin(RBD)::EGFP* [11] and a *sqh-RokKD::GFP* [10](gift from Jennifer Zallen) transgenes. Plasma membrane was visualized using a *UASp-Gap43::mCherry* insertion (chr 3). *fog* gene expression was visualized with an MS2-*fog* pACMAN BAC inserted at the ATTp2 site, located 68A4 on chromosome 3 and the MCP-NoNLS::EGFP from [16]. MCP-NoNLS::EGFP was provided maternally from females *;sqh-Sqh::mCherry;MCP-NoNLS::EGFP*, (insertion at VK18 site on chr 2) or *yw;Histone-RFP;MCP-NoNLS::EGFP* (Bloomington stock #60340) crossed with males carrying the MS2-*fog* BAC and F1 eggs were analyzed. *nos-Gal4* and *67-Gal4* (*mat α4-GAL-VP16*) are ubiquitous, maternally supplied.

For homogeneous expression of Fog, Cta[CA] and Rho1[CA] heterozygotes mothers *;67-Gal4,E-cad::EGFP*[Kin]*,sqh-Sqh::Cherry;/+* were crossed with males carrying the *pUAST-fog*[6], or *pUAST-ctaQ303L* or *UAS-rho1V14* transgene and F1 eggs were analyzed. The presence of the UAS-transgene was estimated on the basis of the phenotype. F1 progeny of males *Y/FM7 twi-Gal4, UAS-GFP;;UAS-fog*[6]*/+* crossed with female *fog*[4a]*/FM7 twi-Gal4 UAS-GFP;67-Gal4, E-cad::GFP*[KIn]*, sqh–Sqh::mCherry/+* was analyzed in Extended Fig. 3g-h. Mutant embryos were identified based on the absence of ubiquitous EGFP expression after imaging.

All fly constructs and genetics are listed in Supplementary Table 1.

## Constructs and transgenesis

MS2-Fog construction: the *fog* gene was modified in its 3'-UTR region (283 bp downstream the stop codon) by inserting 16 MS2 repeats (gift from Thomas Gregor[16]). A pACMAN BAC clone (CH321-09M06) which encompasses the 30kb of the *fog* gene along with 47kb upstream and 28kb downstream regions was modified by recombineering[36]. The recombined BAC was inserted in the genome at the attp40 landing sites (Chr2, 25C6), using PhiC31 mediated site-specific insertion transgenesis (BestGene, Inc.).

*sqhP*-sqh::mK2 construction: the *sqhPa*-sqh::mKate2 expression vector was generated using a *sqhP*-sqh::mCherry modified vector (kind gift from A. Martin[8]), a pCasper vector containing a *sqh* minimal promoter. A PhiC31 attB sequence was inserted downstream the white gene of the *sqhP* vector at the AfeI restriction site to perform PhiC31 site specific transgenesis. To build the *sqhPa*-sqh::mKate2 transgene, the Open Reading Frame (ORF) of mCherry was replaced by that of mKate2.

## RNA interference and drug injections

dsRNA probes directed against *fog* were prepared and injected at a final concentration of 5 µM in embryos less than 1 h old as previously described[23,37].

α-Amanitin (from Sigma-Aldrich) was injected at a concentration of 500 mg/ml in embryos at the end of cellularization around 5 min prior imaging. The Rok inhibitor H-1152 (Enzo Lifesciences) was injected at a concentration of 40 mM in embryos either at the end of cellularization around 5

min before imaging or at stage 7 during imaging using an InjectMan4 micromanipulator and a FemtoJet 4i microinjector from Eppendorf directly installed on the imaging microscope.
Dextran injections were performed in the perivitelline space using Dextran 647 Alexa Fluor, 10000 MW, Anionic, Fixable from Thermo Fisher Scientific at a concentration of 1 mg/ml. Embryos were injected at stage 6 or 7 directly on the imaging microscope and imaged after few minutes (~2min) to allow diffusion of Dextran in the perivitelline space.

## Live Imaging

For live imaging embryos were prepared as described earlier[38] and imaged at stage 6 or 7 in the dorsal and posterior region for 10 to 60 min at room temperature (22°C) depending on the experiment. Most time-lapse imaging was performed with a dual camera spinning disc (CSU-X1, Yokogawa) Nikon Eclipse Ti inverted microscope (distributed by Roper) using a 20X/N.A. 0.75 water immersion, 40X/N.A. 1.25 water immersion or a 100X/N.A 1.4 oil-immersion objective depending on the experiment (20X or 40X magnification for tissue-level resolution and 100X magnification to obtain cellular level resolution). Dual color imaging of EGFP and mCherry/mKate2 FPs was performed by simultaneously exciting the fluorophores with a 491 nm and a 561 nm laser, and using a dichroic mirror to collect emission signals on two cameras.
Live imaging of laser ablation and laser cauterization experiments was performed with an Eclipse TE 2000-E microscope equipped with a spinning disc Ultraview ERS (Perkin-Elmer) using a 40×/N.A. 1.25 water-immersion, or a 100×/N.A. 1.4 oil-immersion objective. Dual color imaging of EGFP and mCherry was performed sequentially using a single camera by rapidly switching the excitation lasers (491 nm and a 561 nm) and emission filters.
For live imaging with 40X magnification z-series of 33-40 planes (spacing 0.8 µm) spanning ~30µm from the cell apex were acquired with a frame rate of 20s or 30s per frame. For live imaging with 100X magnification, z-series of 2-12 planes spanning 1 to 6 µm were acquired with a frame rate of 1-15s/frame. For laser ablations a single plane was imaged at a frame rate 0.5s/frame. Laser powers were measured at every imaging session and kept constant during the experiment.
Two-photon imaging of mid-sagittal sections (Fig. 4i) was performed with a Nikon confocal equipped with a Nikon 25X/N.A. 1.1 objective. A single section was acquired at a frame rate of 3s/frame.

## Generation of tissue fences by laser cauterization, and laser ablations

Tissue fences were generated within the dorsal epithelium along the Medio-Lateral (ML) embryonic axis at ~30% Embryo Length (EL) from the posterior as previously described[23]. Briefly, tissue cauterization and stitching to the vitelline membrane was obtained by focusing a near-infrared (NIR, 1030nm) laser with a 60X/N.A. 1.2 water-immersion Plan Apo VC, Nikon objective on the apical side of the embryonic blastoderm (~1–2 µm above adherens junctions) with an average power of 150 mW at the back aperture of the objective. To generate fences the stage was moved at a constant speed of 15–17 µm/s.
Line ablations were performed on the dorsal epithelium of embryos at stage 7 as previously described[23]. 20 µm line ablations were generated by moving the laser beam along the AP or ML axis within a region proximal (5-30 µm from the furrow) or more distal (60-100 µm from the furrow) to the invaginating furrow.

## Antibody staining

Embryos were fixed with 4% formaldehyde for 20 min, devitellinezed by shaking in Heptane/Methanol, and then stained according standard procedures[39]. Fog was detected with a Rabbit antibody anti-Fog (1:1000; gifted by Sumusu Hirose[40]), Neurotactin with a mouse

monoclonal antibody (1:100; BP-106 supernatant from DSHB), Tll with an anti-Tll polyclonal guinea pig antibody (1:250; [41], gifted by Cedric Maurange) and a chicken anti-GFP antibody was used to detect Sqh::EGFP (1:1000, AVES-GFP 120). The anti-Tll antibody was pre-adsorbed by incubation ON at 4C with fixed embryos less than 1h old. Secondary antibodies conjugates with Alexa488, Alexa555 and Alexa647 (from MoBiTec) were used 1:500. Stained embryos were mounted in Aqua-Polymount (Polysciences) and imaged with a Zeiss 510 confocal microscope using a C-Apochromat 40X/NA 1.2 or a 60X/NA 1.4 objectives. Image stacks with spacing of 0.3-0.5 μm were collected and sum projections of 3-7 planes analyzed.

## Image processing, segmentation and cell tracking

E-cad::GFP was used to label outlines and the apical side of the cells. A custom ImageJ macro integrating the Stack Focuser plugin from M. Umorin was used to project (by maximum intensity projection) a limited number of z-planes around the apical plane of cells (focused maximum projections). This resulted in sharper cell outlines and better S/N ratio compared with maximal projections. Briefly the macro uses the Stack Focuser plugin with a kernel size of 30 pixels (~ 6 μm) to identify the apical plane locally in all regions of the image on the basis of the E-cad::GFP signal. Then, only 4 planes for E-cad and 7 planes for MyoII around the identified apical plane are projected. The 2D projected stacks were then segmented and cells tracked as previously described[23] using Ilastik (v1.2) and Tissue Analyzer[42].

## Data analysis

All measurements of fluorescence intensity and cell shape parameters were extracted using the Fiji software and further analyzed with Matlab (including Curve Fitting Toolbox, Image Processing Toolbox, Statistics and Machine Learning Toolbox). To plot data the Igor software or Matlab (extended with custom designed as well the available function UnivarScatter from Manuel Lera Ramírez) were used.

***Measurements of fluorescence intensity in individual cells***

Fluorescence intensities were measured on focused maximum intensity projections (for 40X image stacks) or standard maximum intensity projections (for 100X image stacks).

For individual cells measurements mean and integrated intensities were measured within an ROI obtained by automated segmentation and tracking and then shrunken by 4 or 10 pixels for 40X or 100X images respectively to remove junctional signals. For all images background intensities were subtracted by masking out relevant structures and then subtracting residual intensities. To generate the masks images were first background subtracted using a "rolling ball" algorithm (with a radius of ~6 μm for 40X images and ~1.2 μm for 100X images) and then an intensity threshold was used. Residual background images were smoothened with a Gaussian blur filter with a radius of 0.6-1 μm before subtraction.

Time registration of individual cells relative to MyoII activation was performed using a threshold on MyoII mean intensity.

To extract maximum or minimum values of the integrated intensity (Fig.3f) and contraction rate (Fig.4h), the parameters were smoothened over time with a rolling average using a window of 40sec.

For quantifications of Rho-GTP in Fig. 5 Ani(RBD)::GFP mean intensity was measured manually in circular ROIs of diameter 3.6μm. The rate of Rho1 sensor recruitment was estimated by a linear fit of mean intensity measurements in an interval of 60s before and 60s after injection.

***Measurements of fluorescence intensity in the tissue***

For space-intensity plots, we measure MyoII mean intensity along ML axis and plot it as a function of the distance from the invaginating furrow along AP axis. Mean intensity is measured after

background was subtracted using a "rolling ball" algorithm (with radius 4µm). Junctional signal was removed using the ROIs from cell tracking as described above. The position of the furrow was determined using either the position where the derivative of the standard deviation of the MyoII signal reaches its maximum, or the position where the derivative of the mean of the MyoII signal first exceed its half-maximum. For each time point an average on time was performed within a time window of 20sec (rolling average). For each embryo data are averaged across several time points spanning 5-7 min.

For the scatter plots in Extended Fig.1, we measured mean MyoII and mean ROK or Rho sensor intensity in small regions of the tissue and plot one signal against the other. To do so, 100x movies of MyoII and ROK or Rho sensor where cropped respectively to 36x36µm$^2$ or 25x25µm$^2$ and registered using the Fiji plugin StackReg. Intensity was then averaged in bins of 3.6x3.6µm$^2$ or 2.5x2.5µm$^2$. Measurements of MyoII intensity vs ROK or Rho sensor intensity where plotted for all bins and all time frames (spanning ~5min) and correlation coefficient was calculated. We checked that binning did not affect the correlation.

For tissue level MyoII polarity measurements, we used focused maximum intensity projections of embryos 10min after primordium activation. We subtracted background using a 'rolling ball' algorithm with radius 10µm and a threshold. We then measured mean MyoII intensity in rectangular ROIs in the active zone I(az) (which correspond to the propagation zone for WT and to the primordium for the other conditions) and the inactive zone intensity I(iz) (corresponding to the amniosierosa). The size of the ROIs spanned from ~10x30 µm$^2$ to ~50x80 µm$^2$ according to the visible area of the tissue (in WT the primordium has already invaginated at 10min). We defined polarity to be (I(az)-I(iz))/I(az).

***Reconstruction of initial cell position for kymograph heat maps***

In order to look at the propagation of cell shape and MyoII intensity parameters across the tissue, we elaborated kymograph heat maps to represent in a single graph space (position along the AP axis), time and value of any given parameter (area, integrated intensity, etc.). Measurements from cell tracking are used. Since at first approximation the phenomenon is symmetric along ML axis, we average data along this axis (Ext. Fig.1a and 1c). To remove the impact of cell movements (and estimate actual propagation from one cell to the next) we use initial coordinates for coordinates in the space axis (Registered kymograph Ext. Fig.1d). To do so, we bin individual cells in 2µm-wide bins according to their initial position along AP axis (their center position at time *t0* as found from tracking). If a cell *x* is not present in the first frame and appears only on frame number *tx*, we infer its initial position by extrapolating from initial positions of all cells present at *tx* and in the first frame. For any bin the median of the given parameter across all cells of the bin is used for color-coding. This representation can be used on any parameter measured from cell: integrated intensity, area, velocity, etc and enables to monitor propagation within the tissue independently of tissue deformation.

***Measurements of the wave speed***

We measured the wave speed either automatically from tracked cells data, or, when segmentation and tracking were not performed, by manual counting.

Automatic measurement:

Speed of the wave can be measured either in the reference frame of the tissue (or initial frame reference, i.e. time t0) as defined for kymograph heat maps, or in the embryo reference frame. In Fig.4d, we compare the speed of the wave across the tissue (from one cell to the next) in conditions where tissue deformations are very different, hence we use the first method. In Fig.3g, we compare the speed of the wave set by extracellular diffusion in conditions where deformations are very similar, hence we use the second method.

To measure the speed of the MyoII activation wave in the reference frame of the tissue (initial frame reference), we first binarize the kymograph heat maps of the mean intensity of MyoII, select manually the region corresponding to the propagation and then perform a linear fit of the positions

of MyoII activation as a function of their time of activation (Fig.4d). Activation is defined by mean MyoII intensity crossing a threshold. We proceed similarly for measuring the speed of the mechanical cycle using cell apical area and cell position along the apico-basal axis of the tissue (position in z), we use the reconstructed kymograph heat maps displaying cell apical area, or the position in z of the cadherin belt as a proxy for the cell surface (Fig.4j,k,l).
To measure the speed of the MyoII activation wave in the reference frame of the embryo, we perform a linear fit of the cell position at the time of MyoII activation as a function of time of activation (Extended Fig.3e). Here the positions are read directly from the microscopy images, which is the frame of the embryo. Activation is defined by mean MyoII intensity crossing a threshold. Such a reference frame is used in Fig.3g where we are interested in diffusion of Fog in the perivitelline fluid.
Manual measurement:
To obtain the wave speed in the reference frame of the tissue (initial frame reference), we manually recorded the time of MyoII activation cells of the propagation zone belonging to 3-4 rows of cells aligned along AP-axis in each embryo. For each embryo we averaged over the different rows, and different embryos were averaged to obtain plots of the number of cells having activated MyoII along an AP row as a function of time. Time 0 is defined as the time of activation of the first cell in the propagation zone. This measurement is used in Fig. 2f, and using Rho sensor instead of MyoII, in Fig. 3b. We also extract the number of cells having activated MyoII within 20min from these measurements (Fig.3k).

***Measurements of tension***
The average tissue tension in Extended Fig. 4, proportional to the initial outward velocity after line cuts, was measured as previously described[23] by particle image velocimetry (PIV).

## Simulations of wave propagation by diffusion or mechanical feedback
Full details on the simulations can be found in the Supplementary Methods.

## Embryo synchronization
Embryos synchronization was performed to compare different mutant conditions with WT embryos and to register embryos in developmental time before pooling and averaging. Synchronization is based on two developmentally-regulated events: 1) the disappearance of MyoII from the cellularization front at the basal side of cells and 2) the onset of cell divisions in the dorsal posterior ectoderm (see Ext. Fig. 2d). Both events are independent of morphogenesis of the posterior endoderm. Time T0 is then defined as the onset of MyoII recruitment and apical constriction in WT embryos.
For immunofluorescence experiments in fixed samples embryos staging was determined manually on the basis of similarity with events observed in time-lapse experiments.

## Statistics
For all experiments data points from different cells/embryos from at least 2 independent experiments were pooled to estimate the mean, s.d. and s.e.m. values plotted. All of the *P* values are calculated using a two sided non-parametric Mann–Whitney test (Matlab statistic toolbox) except in Fig.3j where P values are calculated using a one-sample t-test (0 as reference value, Matlab statistic toolbox). No statistical method was used to predetermine sample size. The experiments were not randomized, and the investigators were not blinded to allocation during experiments and outcome assessment.

## Repeatability

All measurements were performed in 1–11 embryos. In experiments where embryos are not injected we consider each embryo as an independent experiment. In drug and dsRNA injection experiments the number of independent experiments is defined as the number of independent injections. Representative images, which are shown in Figs 1-5 and Extended Figs 1-5 were repeated at least twice and up to more than ten times.

## Data Availability

The authors declare that the data supporting the findings of this study are available within the paper and its supplementary information files. Raw image data are available upon reasonable request.

## Code availability

The custom codes used to process images analyze data and run simulations are available upon request.